RICE UNIVERSITY

Universality in the Equilibration of Quenched Yukawa One Component Plasmas

by

Thomas Langin

A Thesis Submitted
in Partial Fulfillment of the
Requirements for the Degree

Master of Science

Approved, Thesis Committee:

Thomas C. Killian, Chair
Professor of Physics & Astronomy

F. Barry Dunning
Sam and Helen Worden Professor of
Physics & Astronomy

C.H. Kiang
Associate Professor of Physics &
Astronomy and Bioengineering

Houston, Texas

April, 2015

ABSTRACT

Universality in the Equilibration of Quenched Yukawa One Component Plasmas

by

Thomas Langin

A Yukawa one-component plasma (OCP) is an idealized model in which particles interact through a $1/r$ potential with an additional exponential falloff with length scale κ^{-1} expressed in units of the average interparticle spacing. This model is used to approximately describe a wide range of physical systems, especially strongly coupled plasmas; i.e., those which have $\Gamma \geq 1$, where Γ is the ratio of the Coulomb interaction energy between neighboring particles to the kinetic energy per particle. All dynamics and physical properties in Yukawa OCPs are expected to be universal in κ when expressed in appropriate scaled units.

We study a particularly clean realization of the Yukawa OCP, an ultracold neutral plasma (UNP) created by photoionization of an ultracold atomic gas. The rapid quench to a UNP results in an equilibration process known as Disorder Induced Heating (DIH). Even after DIH the plasma is strongly coupled, with $\Gamma \sim 3$. During DIH, oscillations in Γ^{-1} (i.e. scaled Kinetic Energy) occurring at twice the plasma frequency, ω_{pi}, are observed, possibly indicating coupling to collective modes. Universality is demonstrated by showing that $\Gamma^{-1}(t)$ curves taken at similar κ collapse onto the same curve when plotted vs. $\omega_{pi}t$. We also compare our results to molecular dynamics (MD) simulations. The utility of the universality is shown by using the MD simulations to determine the density from experimental DIH measurements.

Acknowledgements

I would first like to thank my advisor, Tom Killian, for his guidance both in the writing of, and in the research within, this thesis. Without his input, the quality of both would have suffered dramatically. In particular, his ability to edit a confusing mess of an explanation into a concise one which clearly conveys the point to the reader is a gift I'll need to acquire myself so I can use it when I graduate and no longer have him to edit my drafts. I would also like to thank my other committee members, Barry Dunning and Ching-Hwa Kiang, for taking the time to review this thesis.

My partners in the plasma lab, Patrick McQuillen (PhD 2015) and Trevor Strickler, were also instrumental in training me to accomplish the tasks set forth in this thesis. The experimental apparatus and data analysis codes are both very formidable at first glance, and I would never have understood them without their guidance. Conversations with members of the other two experiments in the Killian Lab, "neutral" (Jim Aman and Brian DeSalvo (PhD 2015)) and "rydberg" (Francisco Carmago, Roger Ding, and Joe Whalen) were also essential, as they provided guidance and occasionally a necessary diversion from my own struggles.

My father, Thomas, and mother, Margaret, along with the rest of my family, have always supported me throughout my life's journeys and for that I thank them. I would not be here at Rice today were it not for them. My girlfriend, Rachel, also aided in this work by providing essential love and support. Love you.

Lastly, I would like to thank the funding sources for the plasma experiment: the United States National Science Foundation, the Department of Energy, and the Air Force Office of Scientific Research. My stipend is provided by the National Defense Science and Engineering Graduate Fellowship (NDSEG).

Contents

Illustrations

Chapter 1

Introduction

1.1 Motivation: Strongly Coupled Plasmas

Throughout the last century, many different tools have been developed for studying systems of charged particles, otherwise known as plasmas. The simplest, and least computationally intensive, tool is magnetohydrodynamics (MHD), in which the microscopic effects of collisions between particles are neglected and only bulk properties are considered (i.e. a fluid treatment). This is valid in the regime where the collisional effects are dominated by many weak "small angle" scattering events which occur on a timescale far shorter than the system timescale ($t_{sys} = L/v_T$, where L is the size of the system and v_T is the thermal velocity). In this case, collisions serve only to isotropize and thermalize the plasma.

One necessary, but not sufficient, feature a plasma must have to be well described by MHD is:

$$\Lambda = \frac{4\pi}{3} n \lambda_D^3 = \frac{4\pi}{3} n \left(\frac{k_B T \epsilon_0}{n e^2} \right)^{3/2} = \frac{1}{(3\Gamma)^{3/2}} \gg 1 \tag{1.1}$$

where n is the density, $\lambda_D = \sqrt{k_B T \epsilon_0 / (n e^2)}$ is the Debye screening length, beyond which collisions are ineffective, and:

$$\Gamma = \left(\frac{3}{4\pi} \right)^{2/3} \frac{n^{1/3} e^2}{3 k_B T \epsilon_0} = \frac{e^2/(4\pi\epsilon_0 a)}{k_B T} \tag{1.2}$$

where $a = \left(\frac{3}{4\pi n}\right)^{1/3}$ is the average interparticle spacing. In other words, for MHD to

work well there must be many particles within one "Debye sphere" ($\Lambda \gg 1$) or, equivalently, the ratio of the potential energy between neighboring particles ($e^2/(4\pi\epsilon_0 a)$) to the kinetic energy ($k_B T$) must be very small ($\Gamma \ll 1$).

If close collisions have a small, but non negligible effect (i.e. if there are a moderately large number of particles in a Debye sphere) , they can be accounted for using "kinetic" models, where the effects of particle interactions on the phase-space distribution function $f(x, v, t)$ are modeled through collision rates. Theories yielding analytic expressions for these rates (e.g. the Landau-Spitzer theory of collisions) treat the effect of the interactions as a small perturbation.

However, in so-called "strongly coupled plasmas" (SCPs), for which $\Gamma \gtrsim 1$, we must take a step further and treat the cloud as N individual particles with dynamics determined by some interaction potential. These plasmas are no theoretical abstraction; examples include astrophysical objects such as the cores of gas giant planets and white dwarf stars. Laboratory plasmas such as the plasmas produced in inertial confinement fusion (ICF) experiments and, as we'll explain in Chapter 2, plasmas created from photoionization of a laser-cooled gas (ultracold neutral plasmas, or UNPs) can also be in this regime, as illustrated in Fig. 1.1.

1.2 The Yukawa OCP Model

In order to make any progress in solving the equations of motion for the N particles within the plasma, we need to determine a model for their interaction potential. In the One Component Plasma (OCP) model, the dynamics of one of the species (typically the electrons), are neglected, hence the moniker "One Component Plasma". That species is instead treated as a neutralizing background which rapidly adjusts to screen the interactions between the other, slower, component (typically ions). In

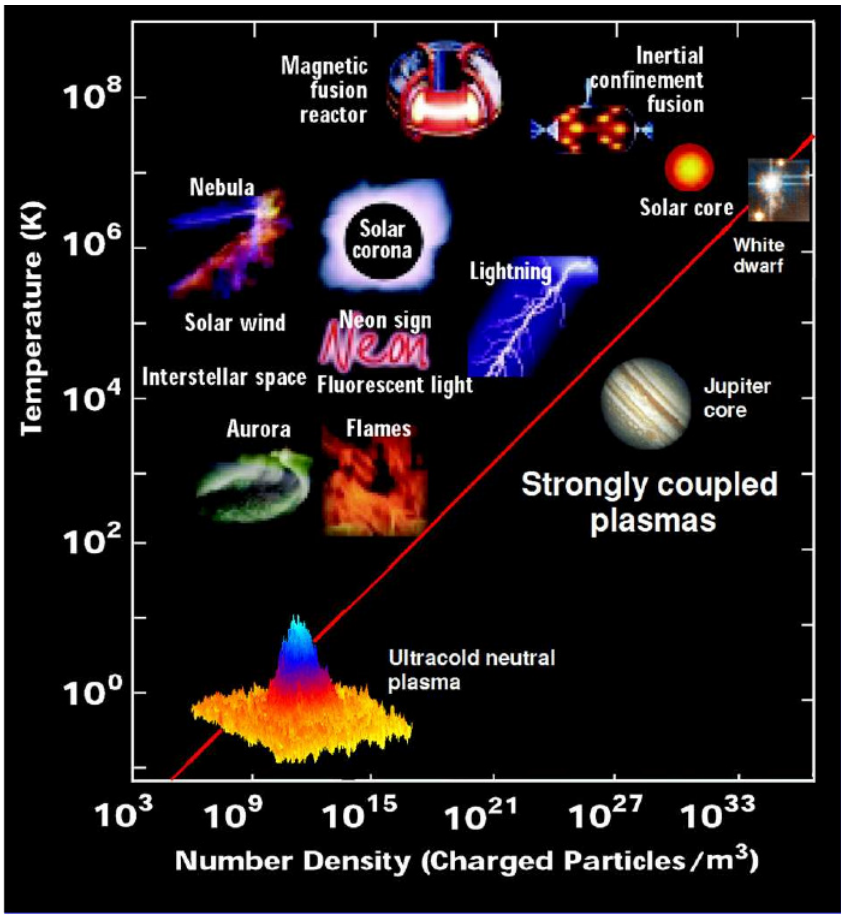

Figure 1.1 : Various plasmas plotted on $n - T$ phase diagram. The red line denotes $\Gamma = 1$. Adapted from [15]

such a plasma, it can be shown that the ions interact through:

$$V(\vec{r}_i, \vec{r}_j) = \frac{(Ze)^2}{4\pi\epsilon_0 a}\frac{a}{r_{ij}}\exp\left[-\frac{a}{\lambda_D}\frac{r_{ij}}{a}\right] = \frac{(Ze)^2}{4\pi\epsilon_0 a}\frac{\exp[-\kappa\tilde{r_{ij}}]}{\tilde{r_{ij}}} \tag{1.3}$$

where $r_{ij} = |\vec{r}_i - \vec{r}_j|$ is the distance between particles i and j, Ze is the ion charge, $\lambda_D = \sqrt{\frac{k_B T_e \epsilon_0}{ne^2}}$, T_e is the electron temperature, $n = n_i = n_e$ is the plasma density, $\tilde{r_{ij}} = r_{ij}/a$ is the distance scaled by the interparticle spacing, and $\kappa = -a/\lambda_D$ is called the "screening parameter".

This is a specific case of the Yukawa interaction:

$$V(\vec{r}_i, \vec{r}_j) = \frac{k \exp[-r_{ij}/\lambda]}{r_{ij}} \tag{1.4}$$

where k describes the strength of the interaction and λ describes the length scale of an additional exponential falloff in the strength of the interaction. This potential was developed by Hideki Yukawa in 1935 to describe interactions mediated by the exchange of massive particles (e.g. the strong force) [21], but, as we showed above, it also applies to screened Coulomb interactions in a OCP. Plasmas which are modeled accurately by Eq. 1.3 are thus known as Yukawa OCPs.

1.2.1 Ultracold Neutral Plasmas: A clean realization of the Yukawa OCP

UNPs are very accurately described by the Yukawa model. They will be discussed in detail in Chapter 2; here we just provide a brief overview. They contain just two components: electrons and singly-ionized atoms (in our experiment, Sr^+) or molecules. Electron temperatures range from 1-1000 K, leading to thermal velocities $v_{Te} \sim 1000-10000\,\mathrm{m/s}$ and $\Gamma_e \sim 0.005-0.2$. On the other hand, the ion temperatures are on the order of 1 K, leading to thermal velocities $v_{Ti} \sim 10\,\mathrm{m/s}$ and $\Gamma \sim 1$. Since we are only interested in the ion dynamics, and $v_{Te} \gg v_{Ti}$, we can effectively ignore the electron motion and treat the electrons simply as a neutralizing background which moves rapidly enough to screen the ion interactions. Of course, this is what is required for the Yukawa OCP model to be accurate.

The Yukawa model can also be applied to the other strongly coupled plasmas we've discussed, such as the cores of gas giant planets and white dwarf stars and ICF plasmas, although for these systems one must occasionally take into account electron degeneracy, as often times $k_B T_e \leq E_f$, where E_f is the Fermi energy. Also, while all ions in UNPs have charge $Z = 1$, ions in these other systems can be in various

multiply ionized states, further complicating (but not invalidating!) the application of the Yukawa model. For these reasons (among others, such as slower timescales and the diagnostic tools available for UNPs, which are discussed in Chapter 2), UNPs are an ideal system for studying the physics of a Yukawa OCP.

1.3 Quench Dynamics in the Yukawa OCP: Disorder Induced Heating

In this thesis, we study the equilibration of a UNP immediately after photoionization. We do this by measuring the average kinetic energy of the ion component of the plasma at different stages during the equilibration process. This is, effectively, a study of equilibration in a strongly coupled Yukawa OCP after a rapid quench in κ from $\kappa = \infty$ (i.e., the non-interacting ultracold gas) to $\kappa = \kappa_f(n, T_e)$, where n and T_e are experimentally controllable parameters. We discuss the results of our experimental study in Chapter 3. However, as the theory pertaining to the quench dynamics is already somewhat developed, we will introduce it here.

The quenching process introduces energy to the system, all of which is initially stored as interaction energy between the repulsive ions. As a result of this change in the potential landscape, close groupings of ions begin to move away from each other. This introduces spatial correlations into the plasma; such spatial correlations are a hallmark of strongly coupled Yukawa OCPs, and of strongly coupled systems (e.g. liquids and solids) in general [13]. The development of the spatial correlations reduces the energy stored in the interactions; by conservation of energy this causes the thermal energy of the plasma to increase. For this reason, this process is often referred to as "Disorder Induced Heating" (DIH), as it stems from the development

of spatial order in an initially disordered plasma.

The temperature of the plasma after heating can be computed simply by determining the difference in the interaction energy before and after the correlations develop; by conservation of energy $\frac{3}{2}Nk_BT_{DIH} = U_{int}(t=0) - U_{int}(t\to\infty)$, assuming that the initial temperature of the gas can be neglected ($T_{gas} \sim 10\,\mathrm{mK}$, which is more than an order of magnitude below typical T_{DIH} values, as we shall soon see). The amount of interaction energy per particle in a spatially correlated system can be determined by (see Appendix A for a full derivation):

$$\frac{U}{N} = \frac{3}{2}\int_0^\infty g(\tilde{r})V(\tilde{r})\tilde{r}^2 d\tilde{r} \tag{1.5}$$

where $V(\tilde{r})$ is the interaction energy (Eq. 1.3 for a Yukawa OCP) and $g(\tilde{r})$, the radial distribution function, is a weighting factor corresponding to the likelihood of different ion pair distances occurring within the plasma.

The radial distribution function simply reflects how local density near any particle (taken to be at the origin) is modified by the correlations: $n_{local}(r) = g(r)n$. For example, in a non-interacting system $g(r) = 1$, meaning that having a particle at the origin doesn't effect the locations of any other particle. In contrast, for a lattice produced by a very strongly interacting system, we'd have something like $g(r) \propto \delta(r-r_1)\delta(r-r_2)...$ where r_1 is the nearest neighbor separation, r_2 is the next nearest neighbor separation, etc.

For systems in between those two limits, $g(r)$ is more difficult to calculate. However, it can be shown that for plasmas the form of $g(r)$ depends solely on Γ and κ (see Appendix A for the proof), and I'll henceforth refer to it as $g(r,\Gamma,\kappa)$. The equilibrium form of $g(r,\Gamma,\kappa)$ is known through molecular dynamics (MD) simulations [7]; Figure 1.2 shows $g(r,\Gamma,0)$ for several values of Γ. The clear features are the depletion

of close pairs occurring even at moderate ($\Gamma \sim 3$) coupling and the further development of spatial structure in the form of oscillations in $g(r)$ as interactions increase ($\Gamma \gtrsim 20$):

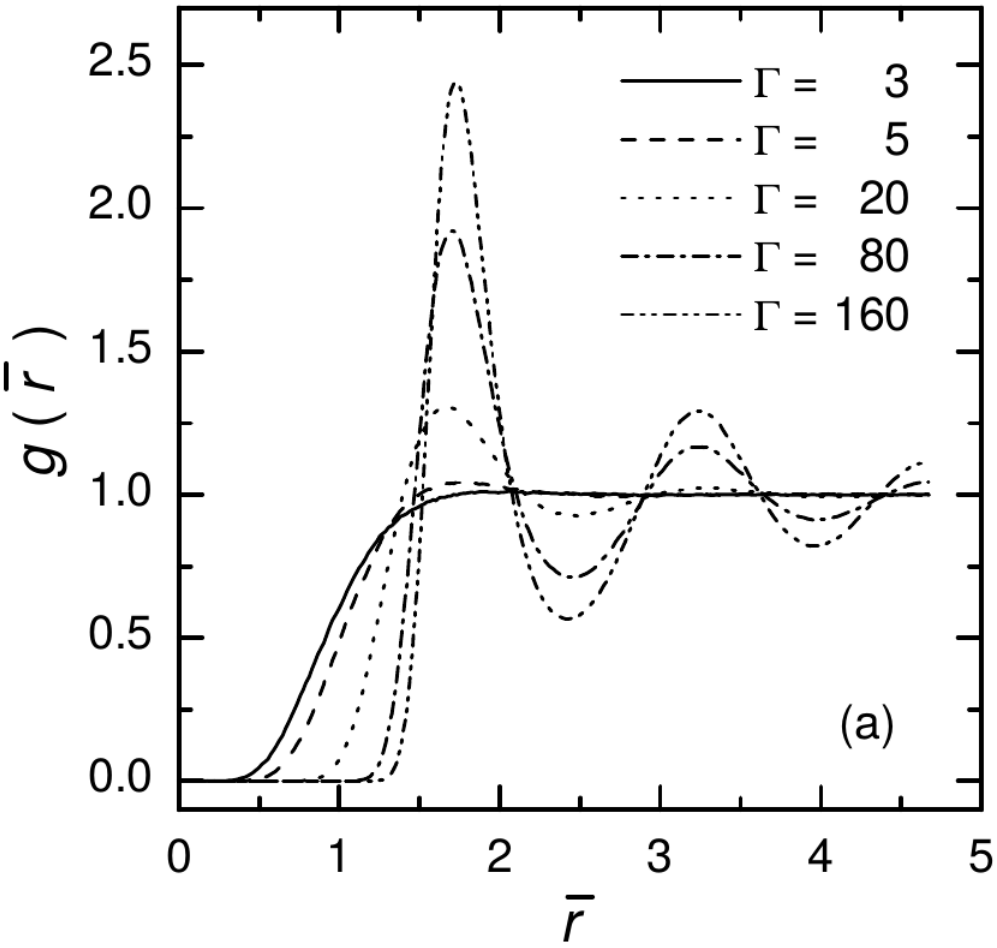

Figure 1.2 : Simulation data on $g(r)$ ($\bar{r} = r/a$) for $\kappa = 0$. More structure becomes evident as Γ increases. Figure from [7]

We now have everything we need to calculate the change in interaction energy due to the quench; from Eq. 1.5 we have:

$$\frac{U_f - U_i}{N} = \frac{3}{2}\int_0^\infty (g_f(\tilde{r}) - g_i(\tilde{r}))V(\tilde{r})\tilde{r}^2 d\tilde{r} = \frac{3}{2}\frac{e^2}{4\pi\epsilon_0 a}\int_0^\infty (g_f(\tilde{r},\Gamma_f,\kappa_f) - 1)\frac{\exp[-\kappa_f\tilde{r}]}{\tilde{r}}\tilde{r}^2 d\tilde{r} \tag{1.6}$$

where subscript i (f) refers to the pre(post)-equilibration values, and I've inserted $g_i = 1$ to reflect the lack of correlations immediately after the quench. By conservation of energy, we then have:

$$k_B T_i - k_B T_f = \frac{e^2}{4\pi\epsilon_0 a}\int_0^\infty (g_f(\tilde{r},\Gamma_f,\kappa_f) - 1)\frac{\exp[-\kappa_f\tilde{r}]}{\tilde{r}}\tilde{r}^2 d\tilde{r} \tag{1.7}$$

which can then be rearranged to yield:

$$\int_0^\infty (g_{eq}(\tilde{r},\Gamma_f,\kappa_f) - 1)\frac{\exp[-\kappa_f\tilde{r}]}{\tilde{r}}\tilde{r}^2 d\tilde{r} = \Gamma_i^{-1} - \Gamma_f^{-1} \tag{1.8}$$

Solutions of the integral in Eq. 1.8 over equilibrium pair-distribution functions have been tabulated in MD simulations [12], and these can be used to determine Γ_f from Eq. 1.8 for a known Γ_i. The integral is negative for all g_{eq}, and therefore $\Gamma_f < \Gamma_i$, meaning that the quench results in heating, as expected.

For our experiment, Γ_i^{-1} can be neglected due to the low initial temperature before equilibration. In this situation, Eq. 1.8 can be solved to give $\Gamma_f(\kappa_f)$, i.e., the post-equilibration value of Γ is uniquely determined by κ_f! This is no coincidence, but rather a specific example of a general phenomenon in Yukawa OCPs, which is that all dynamics and physical properties are expected to be universal in κ when units are scaled appropriately (e.g. length by a). To see why this is the case, we can consider the Hamiltonian of the Yukawa OCP:

$$H = \sum_i \frac{p_i^2}{2m} + \sum_{i\neq j}\frac{1}{2}\frac{e^2}{4\pi\epsilon_0 r_{ij}}\exp[-r_{ij}/\lambda_D] \tag{1.9}$$

Defining the plasma frequency $\omega_{pi} = \sqrt{\frac{ne^2}{m\epsilon_0}}$ and scaled momentum $\tilde{p} = \frac{p}{ma\omega_{pi}}$ we can rewrite Eq. 1.9 as:

$$H = \frac{1}{2}\frac{e^2}{4\pi\epsilon_0 a}\left(\sum_i 3\tilde{p}_i^2 + \sum_{i\neq j}\frac{\exp[-\kappa\tilde{r_{ij}}]}{\tilde{r_{ij}}}\right) \tag{1.10}$$

Clearly, $\frac{e^2}{4\pi\epsilon_0 a}$ is the proper energy scale for the system (note that this is also the factor used in scaling the thermal energy when moving from Eq. 1.7 to Eq. 1.8). Defining $\tilde{H} = \frac{H}{e^2/4\pi\epsilon_0 a}$, we have

$$\tilde{H} = \frac{1}{2}\left(\sum_i 3\tilde{p}_i^2 + \sum_{i\neq j}\frac{\exp[-\kappa\tilde{r_{ij}}]}{\tilde{r_{ij}}}\right) \tag{1.11}$$

which we'll call the "scaled" Hamiltonian (note that if the "Einstein frequency" ($\omega_e = \omega_{pi}/\sqrt{3}$) is used, the prefactor of 3 on the momentum term vanishes. But, we will rescale by ω_{pi} in this thesis).

The form of Eq. 1.11 clearly demonstrates that when units are scaled appropriately, the Hamiltonian for a set of particles with momenta $\{p_i\}$ (if the system is thermalized, this can be taken from a maxwell-boltzmann distribution) and interparticle distances $\{r_{ij}\}$ (which can be taken from $g(r)$) depends solely on κ. Our study of DIH in a UNP then, is a test of this general principle applied to the dynamics of a plasma after a rapid quench to κ_f.

In this thesis, we compare our experimental results to Molecular Dynamics (MD) simulations, which propagate Hamilton's equations of motion using Eq. 1.11 for a set of particles with $\{\tilde{p}_i(t=0)=0\}$ (i.e., setting the initial temperature to zero) and a uniform unweighted set of $\{\tilde{r}_{ij}(t=0)\}$ (reflecting the initial lack of correlations in the ultracold gas). The kinetic energy (in scaled units, $\Gamma^{-1}(t)$) is then determined by the Hamiltonian, which can be directly compared to our temperature measurements.

The details of the comparison are discussed in Chapter 3.

If our hypotheses are correct; namely, that UNPs realize the Yukawa OCP model and that, therefore, the equilibration dynamics should scale with κ_f, we should observe the following results:

- After a sufficient "equilibration time" t_{eq}, the measured value of Γ in both the simulation and experiment should match that predicted by Eq 1.8
- The equilibration process observed in the experiment for a given κ_f (i.e. the dependence of Γ^{-1} on $\omega_{pi}t$) should match the MD simulation data taken at κ_f, regardless of the actual n and T_e which led to κ_f. This could be demonstrated by showing that data taken at dramatically different n and T_e, but with comparable κ_f, collapse onto the curve from the MD simulation.

In Chapter 3 we present our results from the MD simulations and the UNP experiment which verify these hypotheses.

1.4 Roadmap

Chapter 2 will briefly touch on the history of UNPs and why they are a good system for studying the dynamics of strongly coupled Yukawa systems. I'll also discuss how we generate UNPs and use laser-induced fluorescence to measure n and T_i.

In Chapter 3, I present our experimental study of DIH in a UNP. As demonstrated in the previous section, when units are scaled appropriately (i.e. time by ω_{pi}^{-1}, energy by $\frac{e^2}{4\pi\epsilon_0 a}$, etc.), the equilibrium temperature (Γ_{eq}^{-1}) of the system should be uniquely determined by κ_f via Eq. 1.8. Moreover, the evolution of the system towards that equilibrium temperature should also be uniquely determined by κ_f. We demonstrate these features by measuring the temperature evolution of UNPs immediately after

photoionization and comparing our data to MD simulations. We vary n and T_e over orders of magnitude and verify that when the resulting T_i vs t curves are scaled appropriately (i.e. they become Γ_i^{-1} vs. $\omega_{pi}t$ curves), plasmas of equivalent κ match the scaled curves from the MD simulations. We also verify that the final temperature matches that predicted by Eq. 1.8.

Kinetic energy oscillations (KEOs) occurring at $2\omega_{pi}$ are also observed in both the simulations and the data, indicating potential coupling to collective modes. The scaling of the KEOs is also shown to depend only on κ.

Finally, in Chapter 4, the utility of the universality is demonstrated by using the MD simulation to accurately measure the density from experimental DIH measurements.

Chapter 2

Ultracold Neutral Plasmas

Ultracold neutral plasmas (UNPs) have been a topic of interest since they were first created at NIST in 1999 by photoionizing a laser-cooled gas of Xenon atoms, with the photoionization laser tuned just above the ionization continuum. [16] UNPs can also be generated through spontaneous ionization of a dense cloud of Rydberg states [34, 33, 6] or by the photoionization of molecules seeded in a supersonic molecular beam. [27] In our lab, we directly photoionize a laser-cooled gas of Strontium atoms.

Interest in UNPs mostly stems from the fact that their ion component is strongly coupled even after equilibration ($\Gamma_{eq} \sim 3$, see Chapter 3). Thus far, UNP experiments at Rice and elsewhere have been conducted at $n = 10^{14} - 10^{17}\mathrm{m}^{-3}$ (yielding $T_i = 0.4 - 4\,\mathrm{K}$ for $\Gamma = 3$) and $T_e = 10 - 500\,\mathrm{K}$, yielding $\kappa \sim 0.1 - 0.6$. This puts them squarely in the classical (i.e. $k_B T_e > E_f$, where E_f is the Fermi energy) strongly coupled plasma (SCP) regime.

As discussed in Chapter 1, the dynamics of SCP systems are determined by Γ and κ. Therefore, UNPs can be used to study physics in plasmas of similar Γ and κ, even if the densities and temperatures of those plasmas differ dramatically from UNP densities and temperatures. In fact, SCPs that exist in nature, such as the cores of gas giant planets and white dwarf stars, and in laboratory systems, such as inertial confinement fusion (ICF) experiments, tend to have densities greater than $10^{23}\mathrm{m}^{-3}$ and temperatures greater than $10^7\,\mathrm{K}$ (see Fig. 1.1). By the principal of universality,

the dynamics of UNPs can be generalized to these interesting systems to the extent to which they are also classical Yukawa Plasmas (for example, electron degeneracy must be taken into account in white dwarf systems and some ICF experiments).

UNPs have advantages over those systems for studying the physics of strongly coupled plasmas for a few reasons. First, the timescale of the ion dynamics in SCPs is set by ω_{pi}^{-1}, which is $\leq 1\,\mathrm{ps}$ in the astrophysical and ICF plasmas, as compared to $\sim 100\,\mathrm{ns} - 1\mu\,\mathrm{s}$ in UNPs. The longer timescale makes the system more amenable to time resolved measurements of system dynamics. Second, tools often used in the atomic physics community, such as optical pumping and laser-induced fluorescence imaging, can easily be applied to UNP systems. These tools have already been used to study the expansion of a plasma into vacuum [18], ion temperature evolution [5, 2, 23], ion acoustic waves [4], and collision rates [1]. In the future, there is hope that laser cooling can be implemented in UNP systems, which should push UNP research deeper into the strongly coupled regime [31], although this has not yet been realized experimentally.

2.1 Experimental Details

2.1.1 Cooling, Trapping, and Photoionizing Atoms

Before moving into recent DIH studies we will briefly describe the experimental apparatus, a diagram of which can be seen in Fig. 2.1, the plasma diagnostic techniques, and the molecular dynamics simulation techniques. We start with a magneto-optical trap of ^{88}Sr atoms, which operates on the dipole allowed $^1\mathrm{S}_0 \rightarrow {}^1\mathrm{P}_1$ transition at 461 nm ($\Delta_{MOT} = -100\,\mathrm{MHz}$). The cooling transition has a small branching ratio (10^{-5}) into the $5\mathrm{s}4\mathrm{d}\,{}^1\mathrm{D}_2$ state, which decays into the triplet manifold to either $(5\mathrm{s}5\mathrm{p})\,{}^3\mathrm{P}_1$ or $(5\mathrm{s}5\mathrm{p})\,{}^3\mathrm{P}_2$. The former state decays back down into $^1\mathrm{S}_0$ at a rate

$\Gamma = 7.5\,\mathrm{kHz}$, while the latter is a long-lived ($\sim 500\,\mathrm{s}$ for a sample at $0\,\mathrm{K}$, $\sim 100\,\mathrm{s}$ at room temperature due to blackbody radiation [37]) meta-stable state. Atoms falling into this state represents a loss channel for our trap. If we want, we can bring these atoms back into the MOT with 481 nm light, which couples the $(5s5p)^3P_2$ state to the $(5p^2)^3P_2$ state, from which the atom can then decay into the $(5s5p)^3P_1$ state, and then back into the $^1S_0$ state. Fig. 2.2 illustrates the atomic Sr level diagram, along with the decay and repump channels.

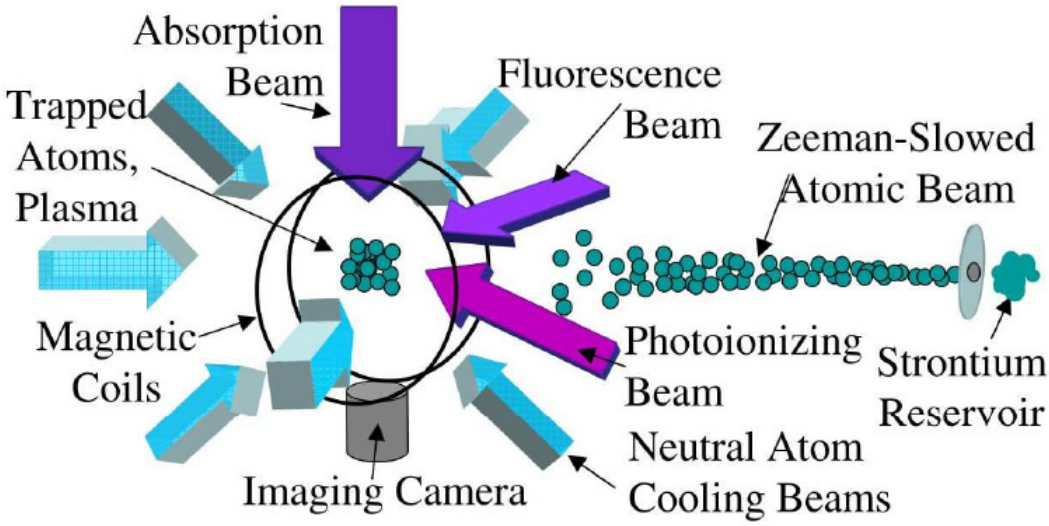

Figure 2.1 : Experimental apparatus for the Plasma Experiment. Zeeman cooled atoms are trapped using a MOT consisting of Anti-Helmholtz coils and 6 detuned laser beams. Plasmas are generated after turning off the MOT by applying intense pulses of resonant 461 nm light (to bring atoms from $^1S_0$ to $^1P_1$), which we call the "push beam", and 405-413 nm light (for photoionization from $^1P_1$), which we call the "photoionizing beam". Ions are imaged either through absorption or fluorescence imaging via the Sr^+ transition at 422 nm (see Fig. 2.3) onto the ICCD camera. Adapted from [36]

The trap typically contains either 1 or 5 billion atoms, depending on whether or not we choose to repump the $(5s5p)^3P_2$ atoms. The trapped atoms have a gaussian

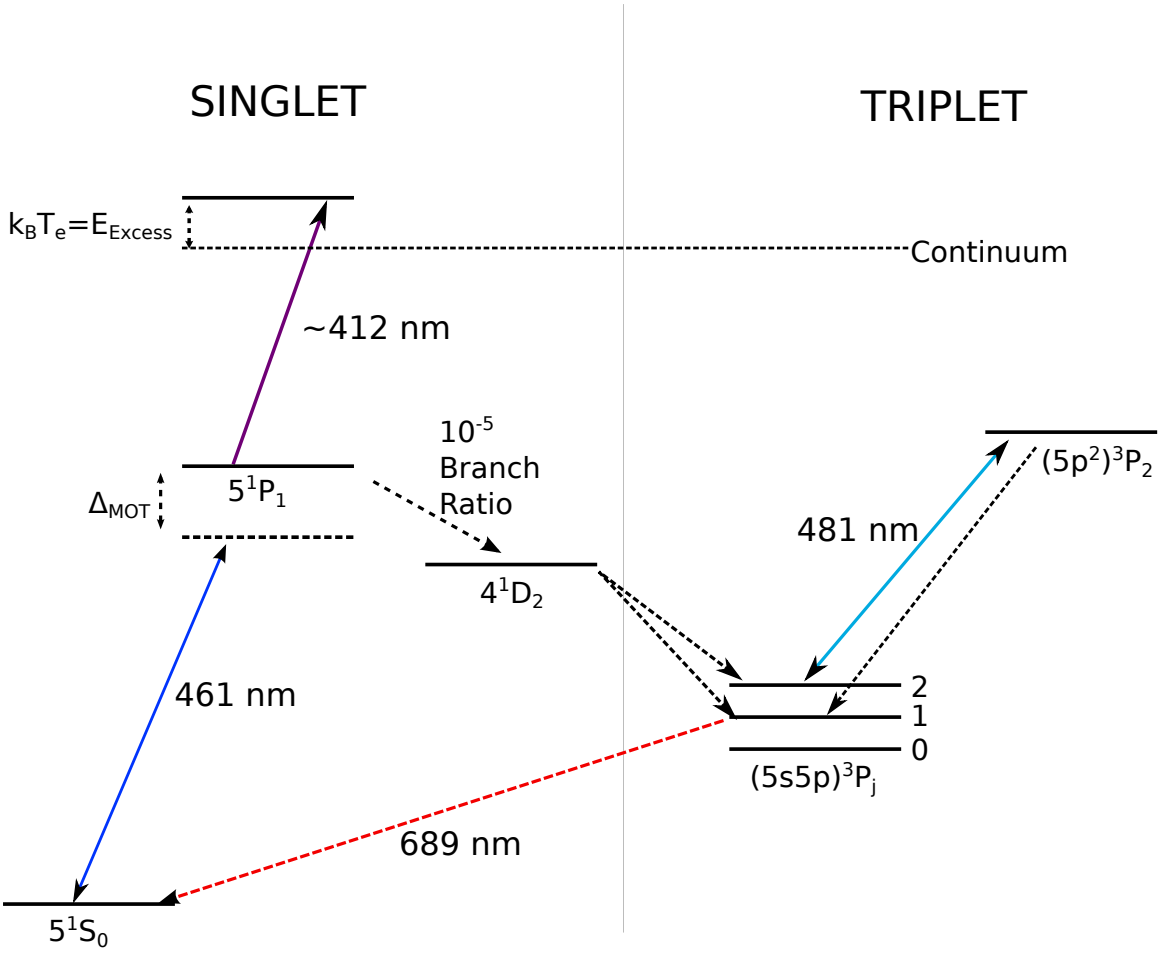

Figure 2.2 : Sr Level Diagram including repumping. Solid lines indicate laser-coupling between states, while dashed lines indicate decay channels.

density profile $n(r) = n_0 \exp(-r^2/2\sigma_{MOT}^2)$ where $\sigma_{MOT} = 1\,\text{mm}$ and n_0 is on the order of 10^{16}m^{-3}, and a temperature $T_{MOT} \sim 10\,\text{mK}$. After the MOT is loaded, the coils are turned off so as not to affect the subsequent plasma dynamics. The beams are also turned off and the atoms ballistically expand into vacuum for $t \gtrsim 500\,\mu\text{s}$ before photoionization.

Photoionization is accomplished through two pulsed beams: a 461 nm beam operating on the cooling transition which we call the "push" beam and an "ionization"

beam tunable from $405 - 413\,\mathrm{nm}$ which brings atoms from $^1\mathrm{P}_1$ to the continuum (the minimum wavelength to ionize from the $^1\mathrm{P}_1$ state is $\sim 413\,\mathrm{nm}$). The former is a pulse-amplified CW laser while the latter is a pulsed dye laser. Both are amplified by dyes pumped with 10 ns pulses of 355 nm light from the 3rd harmonic of a Nd:YAG laser. The tunability of the ionization laser comes from a diffraction grating in a cavity which controls the wavelength the pumped dye emits. This is what allows for control of T_e, as excess ionization energy is converted to electron energy. The plasma retains the same density profile as the MOT, with a peak density determined by the ionization fraction, which can be adjusted by changing the power of the ionization beam. The density can also be changed by allowing the MOT to expand for a longer period of time before applying the photoionization pulses.

2.1.2 Plasma Diagnostics: Temperature and Density Measurement

Unlike alkali atoms which, when ionized, have closed shells much like noble gases, alkaline atoms such as Sr^+ have an outer shell electron, which therefore has hydrogenic optical excitations. The principal transition of Sr^+ from $^2\mathrm{S}_{1/2}$ to $^2\mathrm{P}_{1/2}$ has a wavelength of 422 nm (see Fig. 2.3) and a natural linewidth of $\gamma_0 = 2\pi \times 20.21\,\mathrm{MHz}$. [35] Our main diagnostic tool is laser induced fluorescence (LIF) from a laser tuned near this wavelength. The ions scatter photons from the beam, some of which are then collected and imaged through a 1:1 relay onto an intensified CCD camera (ICCD) with pixel width 12.7μm. Pixels are subsequently binned (4×4 binning) into "superpixels" with a width of 50.7 μm.

The LIF beam is turned on for 2μs, during which the ICCD collects photons for a variable "gate width" which starts at the beginning of the pulse and can be set to last anywhere from 30 ns up to the full 2μ s of the LIF pulse. This minimum gate width of

30 ns determines our temporal resolution. There is some leakage (1/14 branch ratio) into the dark $4^2D_{3/2}$ state (Fig. 2.3), however, as long as the gate width is short enough such that each ion scatters ∼1 photon during the gating, this is not an issue. During our imaging process each ion scatters a photon roughly every 40 ns, so as long as the gate width is not significantly longer than that we need not consider effects due to optical pumping into the dark state.

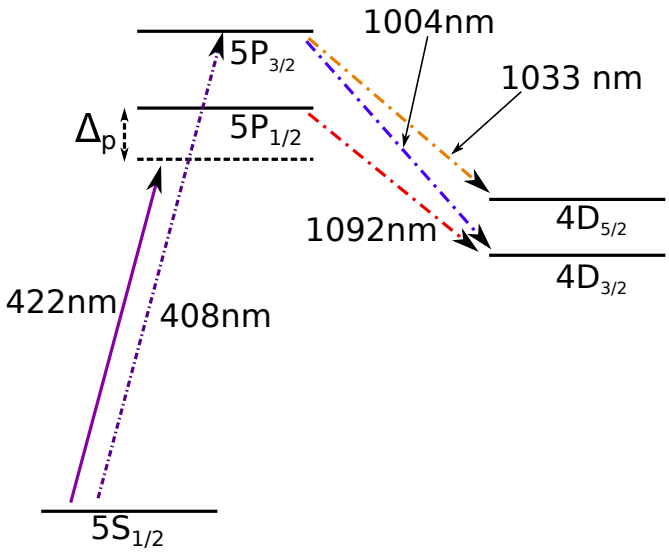

Figure 2.3 : Sr^+ level diagram. We image on the 422 nm transition. The branching rate for decay to the "dark" $4D_{3/2}$ state is 1/14 (i.e. one in 14 ions excited to the $5P_{1/2}$ state decays to the dark state)

Since plasma dynamics depend strongly on density, we want to avoid mixing in signal from too large of a spread in density along the unresolvable camera axis. We do this by passing the LIF beam through a 1 mm slit along the camera axis (for typical size $\sigma = 1$ mm, the density varies by $1 - e^{-1/8} = 12\%$ along the camera axis), see Fig. 2.4. This ensures that each pixel contains information from a fixed density (up to the spatial resolution of the camera), even if that density depends on the pixel (e.g. the center pixel will correspond to a higher density than the one 10 pixels right

of center, assuming the plasma is centered on the center pixel). By scanning Δ_p, the detuning of the LIF beam from the imaging resonance, we acquire frequency resolved images ("LIF images") from which density and temperature can be determined.

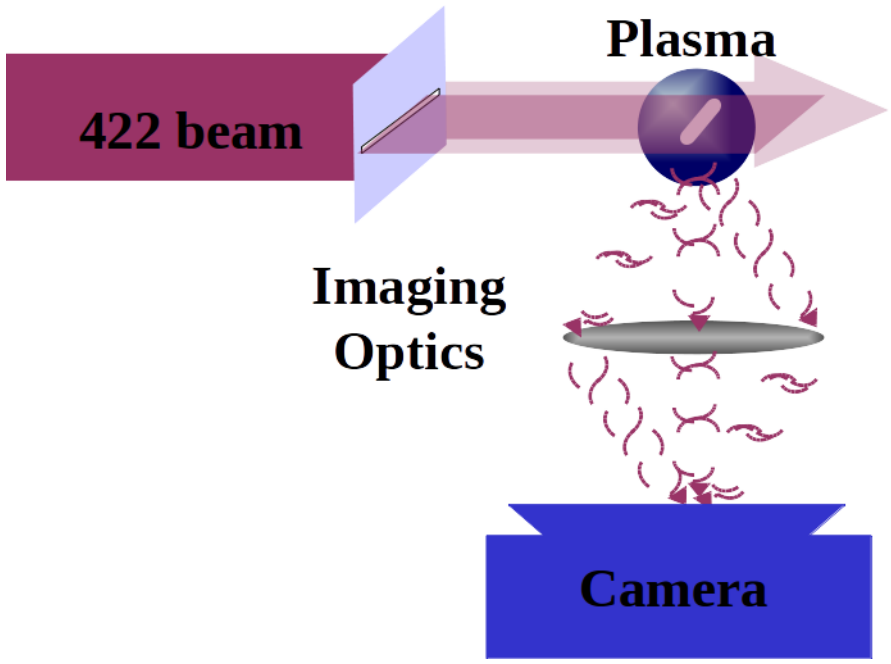

Figure 2.4 : Diagram illustrating LIF Image acquisition. The beam is passed through a slit to avoid mixing in signal from low density regions on the vertical extents of the plasma.

Consider the LIF signal for frequency ν from a plasma of density $n(x, y, z)$ acquired during a gate-time dt. For the pixel located at (x, y) (z being the camera axis) the signal contribution from the box defined by (x, y, z) and $(x + \Delta x, y + \Delta y, z + dz)$, where Δx and Δy are the pixel widths in x and y, is:

$$dS(x, y, z, dt) = C\gamma_0 dt n(x, y, z)\Delta x \Delta y dz f_{exc}(\nu) \tag{2.1}$$

This is simply the total number of photons emitted during time dt from the region ($N_{phot} = \gamma_0 dt N_{Reg} f_{exc}(\nu)$, where $N_{Reg} = n(x, y, z)\Delta x \Delta y dz$ is the number of atoms in

the region and $f_{exc}(\nu)$ is the ν dependent steady-state fraction of ions in the excited state) multiplied by a calibration factor $C = f_{capt}C_{P\to S}$ where f_{capt} is the fraction of emitted photons captured by the camera (this depends on the solid angle of the camera and the spatial pattern of the emission from the excited atoms) and $C_{P\to S}$ is the photon to signal conversion factor.

The tricky part is figuring out what exactly $f_{exc}(\nu)$ is. For fixed detuning $\delta = \nu - \omega$, where ω is the resonance frequency for the LIF transition, an infinitely narrow laser, and stationary atoms, we can solve the optical Bloch equations to find:

$$f_{exc}(\delta, \vec{r}) = \frac{s(\vec{r})/2}{1 + s(\vec{r}) + \frac{4\delta^2}{\gamma_0^2}} = \left(\frac{\gamma_0 s(\vec{r})}{8\sqrt{1+s(\vec{r})}}\right)\frac{\gamma_{eff}}{\gamma_{eff}^2/4 + \delta^2} \tag{2.2}$$

where $\gamma_{eff} = \gamma_0\sqrt{1+s(\vec{r})}$ and $s(\vec{r}) = I(\vec{r})/I_{sat}$ is the "saturation parameter, with $I(\vec{r})$ the intensity of the laser and I_{sat} the saturation intensity of the LIF transition.

However, we must factor in frequency broadening from both the laser's spectrum (which we assume to be lorentzian centered at $\delta = 0$ with width γ_L) and from the doppler-broadening due to the atomic motion (we assume thermalization, so this is a gaussian) centered at $\delta_c(\vec{r}) = v_c(\vec{r})/\lambda$ where $v_c(\vec{r})$ is the bulk motion of the atoms along the laser axis. Taking these broadenings into account gives:

$$f_{exc}(\delta, \vec{r}) = \left(\frac{\gamma_0 s(\vec{r})}{8\sqrt{1+s(\vec{r})}}\right)\left[\frac{\gamma_{eff}}{\gamma_{eff}^2/4+\delta^2} \circ \frac{\gamma_L}{\gamma_L^2/4+\delta^2} \circ \frac{1}{\sqrt{2\pi}\sigma_f}\exp\left(\frac{-(\delta-\delta_c(\vec{r}))^2}{2\sigma_f^2}\right)\right] \tag{2.3}$$

where the $\circ$ indicates convolution with respect to δ, σ_f is the doppler broadened frequency width, and it's written so the convolutions in the square bracket are of normalized distributions.

Now let's consider the total signal for pixel x, y. This will be Eq. 2.1 integrated

over z and δ:

$$S_{Tot}(x,y,dt) = C\gamma_0 dt\Delta x\Delta y \int_{-\infty}^{\infty}\int_{z=-d/2}^{z=d/2} d\delta dz n(\vec{r}) f_{exc}(\delta,\vec{r}) \tag{2.4}$$

where d is the length of the imaging slit (Fig. 2.4). This simplifies dramatically when we consider that the δ integral is over a convolution of three normalized spectra, which by definition will yield 1. Thus, Eq. 2.4 simplifies to

$$S_{Tot}(x,y,dt) = C\gamma_0 dt\Delta x\Delta y \int_{-d/2}^{d/2} dz n(\vec{r}) \left(\frac{\gamma_0 s(\vec{r})}{8\sqrt{1+s(\vec{r})}}\right) \tag{2.5}$$

To go further, we use the fact that intensity profile of the laser is gaussian with $1/e^2$ widths w_z and w_y (x being the laser axis): $I(y,z) = I_0 \exp(\frac{-2y^2}{w_y^2} - \frac{-2z^2}{w_z^2})$. We also have $w_z \gg d/2$ (for our system, $d/2 = 0.5\,\text{mm}$ and $w_z = w_y = 2.5\,\text{mm}$), which allows us to take $s(\vec{r})$ terms outside of the integral over z, thus turning Eq. 2.5 into:

$$S_{Tot}(x,y,dt) = C\gamma_0 dt\Delta x\Delta y \left(\frac{\gamma_0 s_0 \exp(-2y^2/w_y^2)}{8\sqrt{1+s_0\exp(-2y^2/w_y^2)}}\right) \int_{-d/2}^{d/2} dz n(\vec{r}) \tag{2.6}$$

where now $s_0 = I_0/I_{sat}$.

We further simplify by assuming that the density profile is also gaussian: $n(\vec{r}) = n_0 \exp(-\frac{x^2+y^2+z^2}{2\sigma^2})$. Plugging this into Eq. 2.6 gives

$$S_{Tot}(x,y,dt) = C\gamma_0 dt\Delta x\Delta y \left(\frac{\gamma_0 s_0 \exp(-2y^2/w_y^2)\,\text{erf}\left(\frac{d}{2\sqrt{2}\sigma}\right)}{8\sqrt{1+s_0\exp(-2y^2/w_y^2)}}\right) \sqrt{2\pi}\sigma n_0 \exp\left(-\frac{x^2+y^2}{2\sigma^2}\right) \tag{2.7}$$

At this point, we can numerically fit a given image S_{Tot} to Eq. 2.7 with n_0 and σ as free parameters, as all other quantities are known.

That takes care of density. As for temperature, we must consider the signal within a given pixel *as a function of frequency*. So, where before in Eq. 2.4 we integrated over z and δ, we now integrate only over z. This makes things look a little more complicated, since now the convolutions don't just integrate out to unity. We now have:

$$S(x, y, \delta, dt) = C\gamma_0 dt \Delta x \Delta y \int_{-d/2}^{d/2} dz n(\vec{r}) f_{exc}(\delta, \vec{r}) \tag{2.8}$$

We still have $w_z \gg d/2$, which allows us to rewrite $S(x, y, \nu, dt)$ as:

$$S(x, y, \delta, dt) = \left[C\gamma_0 dt \Delta x \Delta y \left(\int_{-d/2}^{d/2} dz n(\vec{r}) \right) \right] f_{exc}(\delta, \vec{r}) \tag{2.9}$$

since the only z dependence in $f_{exc}(\delta, \vec{r})$ comes from $s_0(\vec{r})$, which is allowed to be taken outside the integral in the limit $w_z \gg d/2$. The term in the square brackets becomes a constant whose magnitude can be calculated assuming we've determined the density $n(\vec{r})$ from the camera measurement as discussed prior. So, I'll call that constant $A(\vec{r})$, and therefore we have $S(x, y, \delta, dt) = A(\vec{r}) f_{exc}(\delta, \vec{r})$. To go further, we need to take a closer look at the convolutions within $f_{exc}(\delta)$. It helps to rewrite Eq. 2.3 as:

$$f_{exc}(\delta, \vec{r}) = D(\vec{r}) f_{conv}(\delta, \vec{r}) \tag{2.10}$$

where $D(\vec{r})$ is the constant term in the parentheses of Eq. 2.3 and $f_{conv}(\delta, \vec{r})$ is the convolution in the square brackets of Eq. 2.3. Since $D(\vec{r})$ is also a known constant we can wrap that up into the overall multiplicative factor $A(\vec{r})$, giving $S(x, y, \delta, dt) = A(\vec{r}) f_{conv}(\delta, \vec{r})$ with:

$$A(\vec{r}) = C\gamma_0 dt\Delta x\Delta y \left(\int_{-s/2}^{s/2} dz n(\vec{r})\right)\left(\frac{\gamma_0 s_0(\vec{r})}{8\sqrt{1+s_0(\vec{r})}}\right) \tag{2.11}$$

Now let's look at the convolutions. First, the convolution of two normalized lorentzians with widths γ_1 and γ_2 is just a lorentzian with width $\gamma = \gamma_1 + \gamma_2$. So, f_{conv} becomes:

$$f_{conv}(\delta, \vec{r}) = \frac{\gamma_{Tot}}{\gamma_{Tot}^2/4 + \delta^2} \circ \frac{1}{\sqrt{2\pi}\sigma_f} \exp\left(\frac{-(\delta - \delta_c(\vec{r}))^2}{2\sigma_f^2}\right) \tag{2.12}$$

where $\gamma_{Tot} = \gamma_0\sqrt{1+s_0(\vec{r})} + \gamma_L$. We now have a convolution of a gaussian and lorentzian, which is called a Voigt profile:

$$V(\delta, \gamma, \sigma) = L(\gamma, \delta) \circ G(\sigma, \delta) = \int_{-\infty}^{\infty} L(\gamma, \delta - \delta')G(\sigma, \delta')d\delta' \tag{2.13}$$

Unfortunately, there is no analytic expression for a Voigt profile. Therefore, our final expression for the signal in a pixel at (x, y) as a function of detuning δ is

$$S(x, y, \delta, dt) = A(\vec{r}) \int_{-\infty}^{\infty} d\delta' \frac{\gamma_{Tot}}{\gamma_{Tot}^2/4 + (\delta - \delta')^2} \frac{1}{\sqrt{2\pi}\sigma_f} \exp\left(\frac{-(\delta' - \delta_c(\vec{r}))^2}{2\sigma_f^2}\right) \tag{2.14}$$

with $A(\vec{r})$ given by Eq. 2.11.

The shift in the center velocity of the gaussian distribution due to bulk ion motion $\delta_c(\vec{r})$ is a known quantity, as it stems from the spherically symmetric expansion of the plasma driven by the electron thermal pressure [36]. Therefore, the only unknown in Eq. 2.14 is σ_f, the doppler broadened spectral width due to the thermal velocity distribution ($\sigma_v = \sigma_f\lambda$, where σ_v is the thermal spread in velocities), which is related to temperature through $\sigma_v = \sqrt{k_B T/m}$.

In principle, one could fit a measured camera signal $S(x, y, \delta, dt)$ to Eq. 2.14 with σ_f as a fit parameter for every pixel and determine a "local" temperature measurement

$T(x, y)$. However, this is very unreliable, as the signal within one pixel is small enough to be overwhelmed by statistical fluctuations. Moreover, the local temperature $T(x, y)$ only varies weakly with n ($T_{DIH} \propto n^{1/3}$ and $\omega_{KEO} \propto \sqrt{n}$). Thus, we can sum together pixels corresponding to regions of the plasma with similar density to overcome the statistical fluctuations to measure T, the temperature in the center of the plasma. For the DIH data presented in this thesis, we've considered a 20×21 superpixel region centered at the plasma center as determined by the fit to n_{areal}, corresponding to $1 \times 1.05\,\mathrm{mm}$. The smallest plasmas studied in the thesis have widths of $\sigma = 1\,\mathrm{mm}$, therefore the maximum density fluctuation over the sample is $\sim 1 - \exp(-.5^2) = 22\%$. This leads to a maximal fluctuation of 8% in T_{DIH} and 11% in ω_{KEO} over the region considered.

Naively, this sort of sum would look like:

$$S_{reg}(\delta, dt) = \sum_{i=-10}^{10} \sum_{j=-10}^{10} S(x_i, y_j, \delta, dt) \tag{2.15}$$

where we then fit S_{reg} to Eq. 2.14 to determine T. However, this procedure will yield a drastic over-estimation of the temperature, as the radially dependent expansion velocity gets mixed in via the i terms. This is because of the $\vec{r}$ dependence in $\delta_c(\vec{r})$ in Eq. 2.14: δ_c will vary along x, the axis of the laser. Effectively, you wind up summing 21 spectra, all of which have different center frequencies. To account for this, we need to consider each column separately:

$$S_i(x_i, \delta, dt) = \sum_{j=-10}^{10} S(x_i, y_j, \delta, dt) \tag{2.16}$$

where then each column's signal $S_i(x_i, \delta, dt)$ is fitted to Eq. 2.14 for σ_f. These 21 temperature measurements, T_i, are averaged to determine T. The standard deviation of T_i becomes our statistical error.

Fig. 2.5 shows the severity of the error introduced by fitting Eq. 2.15 for T. The magenta curve is the sum of a 20×15 superpixel grid while the blue, red, and green curves are spectra from a given column of superpixels. Clearly, the magenta curve is wider than the curves from the single superpixel regions: this is due to this convolution of expansion and thermal spread in velocity. A proper temperature measurement from averaging the fits from the 15 columns yields $T = 1.07\,\mathrm{K}$, while fitting the magenta curve yields $T = 2.13\,\mathrm{K}$, obviously a huge difference!

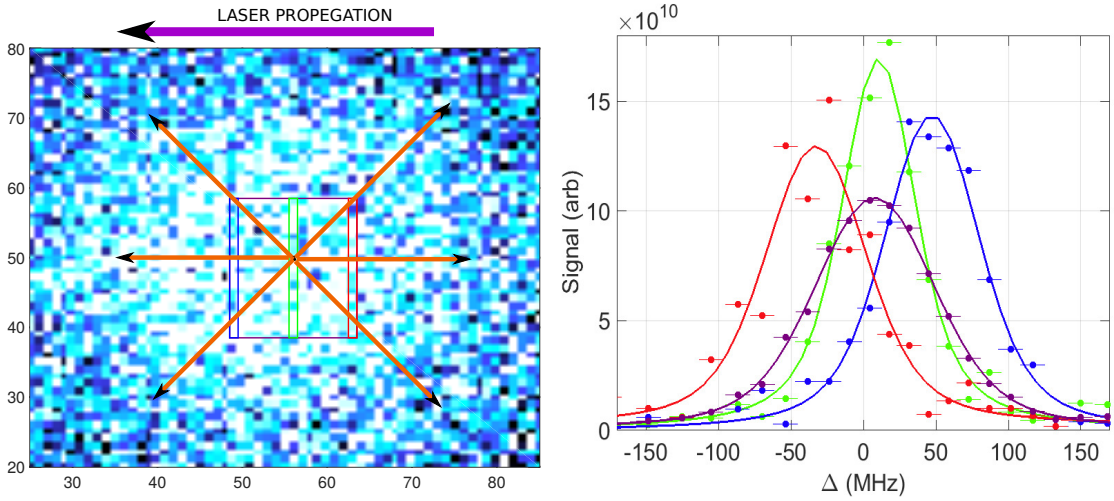

Figure 2.5 : Left: Plasma image with analysis regions. This is the sum of the "stacked" images (i.e. the images at all the different detunings are summed together to create the plasma image). Orange arrows indicate the expansion velocity. Right: Spectra from summing the signal within the corresponding regions for each image in the "stack", normalized such that the integral of each spectra with respect to frequency is constant. The effect of the expansion is clearly demonstrated: the whole red spectrum is redshifted due to the expansion driven bulk motion towards the laser. Vice versa for the blue. The green is roughly centered at zero, as the center of the plasma is unaffected by the expansion. The magenta spectra corresponding to the wide region illustrates the broadening effect of the expansion, demonstrating the need for regional analysis.

Chapter 3

Disorder Induced Heating

Here we present the results of our study of the quench dynamics of a Yukawa OCP resulting from fast photoionization of an ultracold neutral gas. This is also known as "Disorder Induced Heating", or DIH, as touched on in Chapter 1. The structure is as follows:

- Discuss previous studies of DIH and place our work in that context
- Introduce Molecular Dynamics (MD) simulations of DIH at 10 distinct values of κ_f.
- Discuss our experimental study of DIH in detail.
- Compare our experimental study to the MD simulations.

3.1 Previous Studies of DIH

As touched on in Chapter 2, some studies of DIH have already been conducted using UNPs. DIH was theoretically predicted soon after the advent of UNP [9, 29], and was first observed experimentally at Rice in 2004 [5, 17]. In that study, $T_i(t)$ was measured by scanning the frequency of a laser imaged directly onto the camera after passing through the plasma; the plasma profile was reconstructed from the resulting absorption image. This is somewhat inferior to the LIF images we use in this thesis: since the beam passes through the whole plasma (as opposed to through a slit, like

the LIF beam), the contributions to the signal from different density components along the beam get convolved into the image, which can obstruct measurements of DIH, as the process is density dependent. In addition, expansion velocity along the beam axis cannot be separated from thermal velocity, as it can in LIF images. Signal to noise of the absorption image is also worse due to intensity fluctuations within the imaging beam.

Nevertheless, they were able to successfully take these effects into account to obtain measurements of $T_i(\kappa)$ which agreed pretty well with the values predicted from theory (Eq. 1.8). They also observed oscillations in T_i, which we term "Kinetic Energy Oscillations" (KEOS), occurring at roughly $2\omega_{pi}$. These results are reproduced in Fig. 3.1. They also qualitatively observed an increase in the damping of these oscillations with κ.

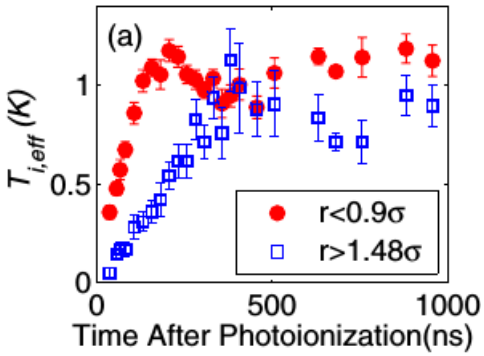

Figure 3.1 : 2004 DIH study. Both data sets are taken from the same plasma; the red data is taken from the central region $r < 0.9\sigma$, where σ is the gaussian width of the plasma, while the blue is taken from the outer wing of the plasma $r > 1.48\sigma$. The frequency of the oscillation increases with density, as expected given the scaling of $\omega_{pi} \propto \sqrt{n}$. Adapted from [5].

DIH, and the KEOs inherent to it, are a specific example of the heating which occurs when ions respond to a rapid increase in interaction energy by developing

correlations [8]. Interest in these equilibration phenomena was initiated by the generation of non-equilibrium plasmas from short-pulse laser irradiation of solid targets. However, such studies were limited to simulations as the short time and length scales associated with these high energy density materials do not lend themselves to easy diagnostics [14, 10, 25, 26, 32, 38]. As discussed in Chapter 2, these limitations do not apply to UNPs, making them a useful tool to study this phenomenon. DIH is also important in electron beam studies, as it provides the ultimate limit on how bright (brightness is inversely proportional to temperature) the beam can be. [22]

KEOs were further explored in a later study by a similar experiment at BYU in 2011. [2] They experimentally determined when the initial peak in the kinetic energy occurred (t_{DIH}) and determined a "measured" plasma frequency (ω_{DIH}) based off the assumption that the frequency of the KEOs was $2\omega_{pi}$ (i.e. $\omega_{DIH} = \pi/(2t_{DIH})$). Comparing this with an independent measurement of the plasma density, and thus of ω_{pi}, they observed that ω_{DIH} approached ω_{pi} as $\kappa \to 0$, however, as κ increased, t_{DIH} became increasingly "late", resulting in a decrease of ω_{DIH} with κ. This was further confirmed qualitatively by MD simulations, however, the experimental results were not directly compared to the simulations. The results of the MD simulations are reproduced in Fig. 3.2. The group conducted a later study which measured $\Gamma_{DIH}(\kappa)$; this too was shown to agree with Eq 1.8 (Fig. 3.3). [19]

In summary, previous studies have:

- Confirmed the scaling of Γ_{DIH} with κ predicted from Eq. 1.8 [5, 19]
- Observed KEOs at $\omega_{DIH} \sim 2\omega_{pi}$, with frequency decreasing with κ [5, 2]
- Qualitatively observed an increase in the damping of the KEOs with κ [5]

However, some topics remain unexplored, such as:

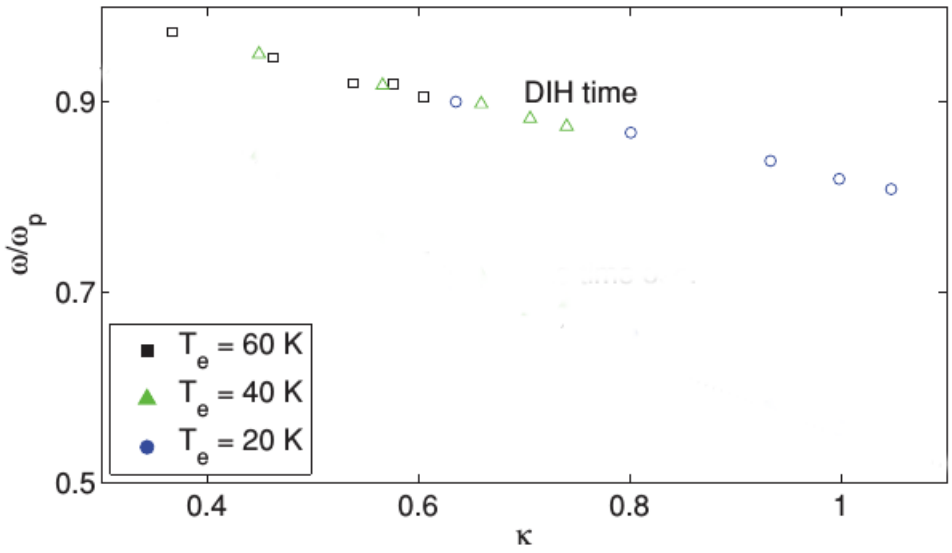

Figure 3.2 : MD results from the 2011 BYU DIH study. The y-axis displays $\omega_{DIH}(\kappa)/2/\omega_p$, where ω_{DIH} is extracted from the t_{DIH} measurements using the simulation data. As $\kappa \to 0$, $\omega_{DIH}/2 \to \omega_p$. The oscillation frequency is observed to decrease with κ. Adapted from [2].

- The dependence of the full $\Gamma_{DIH}(t)$ curve on κ; previous studies have mostly focused only on whether the equilibrium temperature matches Eq. 1.8, not on whether the equilibration process itself matches MD simulations of the plasma evolution after the quench to κ.

- Similarly, can universality in the equilibration dynamics with κ be demonstrated over a wide range of n and T_e? In other words, when $T(t)$ is plotted in scaled parameters $\Gamma^{-1}(\omega_{pi}t)$, do curves taken at similar κ fall on top of each other, regardless of the actual values of n and T_e leading to that κ? If so, does this curve match MD simulations taken at that κ?

- What is the mechanism causing KEOs in the first place, and why does the damping rate of the KEOs increase with κ?

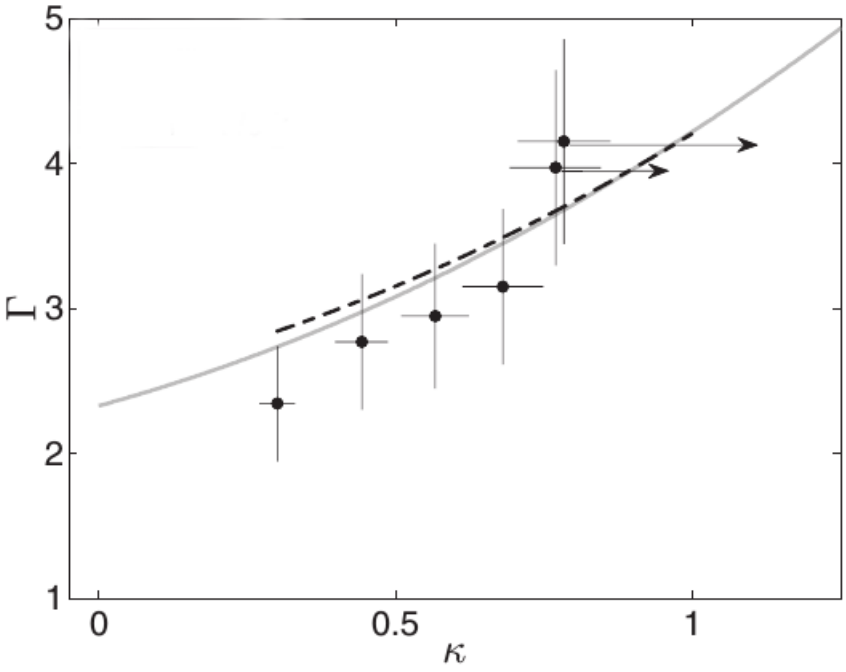

Figure 3.3 : Results of the 2013 BYU DIH study. The gray line is Eq. 1.8, the dotted line comes from MD simulations, and the points are data. The results agree with simulation and theory out to high κ, at which point non-Yukawa OCP physics, such as three body recombination, begins to effect the dynamics.

The work presented in this thesis addresses the first two of these topics; future work will focus on the last topic.

3.2 MD simulations

In order to benchmark our experiment, we enlisted the help of Dr. Thomas Pohl from the Max Planck Institute for Complex Systems to perform MD simulations of the quench dynamics. Starting with a system of $\sim$ 4000 uncorrelated ions at zero velocity, the system is evolved using a leap-frog symplectic integrator technique and periodic boundary conditions to simulate the equations of motion for the Yukawa OCP.

The velocity distributions (in scaled units, $\omega_{pi}a$) are recorded every $0.035\omega_{pi}t$, from which $\Gamma^{-1}(\omega_{pi}t)$, the DIH curve, can be recorded. The simulations were performed at 10 different values of κ, giving us what we've termed a "library" of MD DIH curves (Fig. 3.4). To compare an experimental curve taken at arbitrary κ between $\kappa_{max} = 0.55$ and $\kappa_{min} = 0.12$, we interpolate over the 10 library curves.

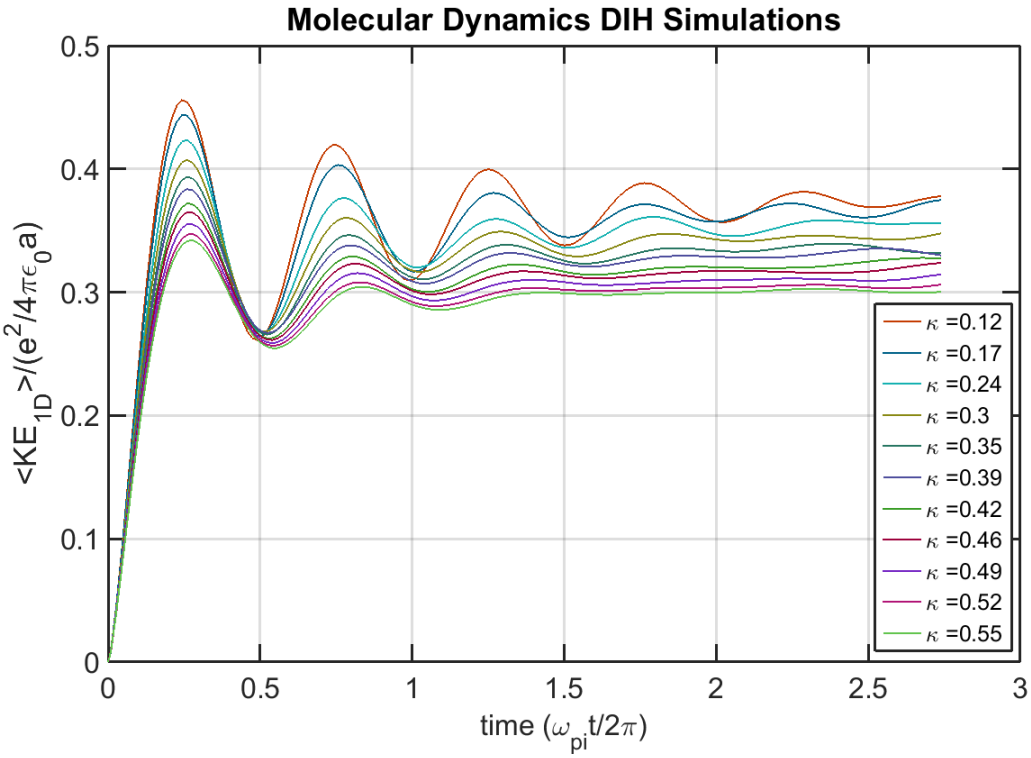

Figure 3.4 : Library of MD DIH curves plotting average 1D kinetic energy per particle $< KE_{1D} >= \frac{m}{2} < v_x^2 >$ vs time. Both axes are in scaled units ($< KE_{1D} >$ scaled by $e^2/(4\pi\epsilon_0 a) = \Gamma^{-1}$, t scaled to $\omega_{pi}t/2\pi$). We interpolate over this library to find the DIH curve for arbitrary κ.

3.2.1 Effect of non-thermalization on comparisons between MD Simulations and Experiments

One important fact we observed when examining the MD simulations is that the ions are not thermalized during the initial stages of DIH, which manifests in a non-Maxwellian velocity distribution; the real distribution is more peaked and has a longer tail, as demonstrated in Fig. 3.5 (this feature was also observed in the MD simulations performed for the BYU experiment [2]). This is reasonable; one would not necessarily expect an equilibrating system to be thermalized. However, since our experimental method for measuring temperatures assumes thermalization (see Chapter 2), we must account for this feature when comparing experimental data to the simulation. If this feature is not accounted for, the measured temperatures would underestimate the actual kinetic energy from the MD curves (Fig. 3.7).

We account for this feature by treating the MD data like our real experimental data. To do this, we must first convert the MD velocity distribution to a doppler broadened frequency distribution. First, we unscale the distributions in Fig. 3.5 by multiplying the scaled velocities by $a\omega_{pi}$ ($v_{real} = v_{scaled} a\omega_{pi}$) using the density, n, of the experimental data with which we want to compare the MD simulation data. We then divide by λ to get the doppler broadened distribution ($v_{real} = \lambda\delta$, so $\delta = v_{scaled} a\omega_{pi}/\lambda$). The doppler broadened distribution is then numerically convolved with a lorentzian, corresponding to our imaging transition, to obtain the "experimental" spectra:

$$S(\delta, \gamma) = \int_{-\infty}^{\infty} L(\gamma, \delta - \delta') MD(\delta') d\delta' \tag{3.1}$$

where $MD(\delta')$ is the doppler broadened frequency distribution from the MD data. This corresponds to what we would see in our data were we to replicate the MD

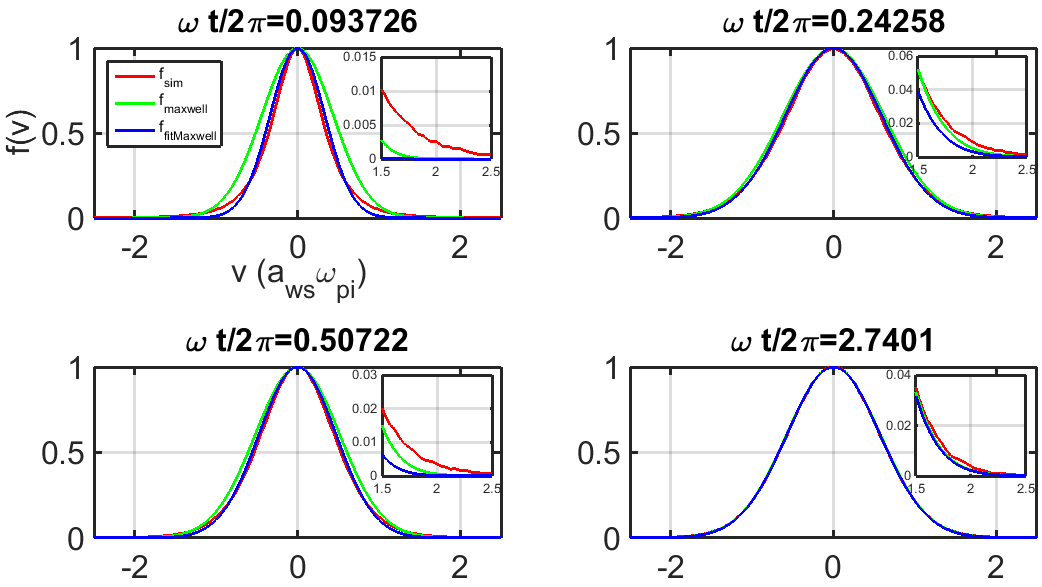

Figure 3.5 : Red: Velocity distribution from the MD Simulations from which the 1D kinetic energy KE_{DIH} can be determined. Green: A maxwellian distribution with $k_BT = KE_{DIH}$. Comparing the red and green curves clearly illustrates the non-thermalized nature of the ions during DIH; a lot of energy is contained in the wings of the distribution (see inset), leading to a narrower profile in the center. Blue: Result from fitting the MD curve to a maxwellian; clearly, this gives an anomalously low measurement of the KE (compare to the green curve). We note that the distribution becomes nearly thermalized at the heating peak ($\omega_{pi}t/2\pi = 0.25$) and subsequently becomes less thermalized at the heating trough ($\omega_{pi}t/2\pi = 0.5$). After sufficient time, the distribution fully thermalizes ($\omega_{pi}t/2\pi = 2.75$)

simulation in our apparatus. We then determine the MD "temperature" by fitting the numerically convolved MD data using Eq. 2.14; this can then be directly compared to the temperature we measure in our experiment. The process of unscaling and convolving the MD data is diagrammed in Fig. 3.6.

Another interesting feature observed in the MD simulations is the long timescale on which Γ evolves to the value predicted by Eq. 1.8 (Fig. 3.7). Unfortunately, we cannot observe this behavior clearly in our experiment since other dynamics, such as

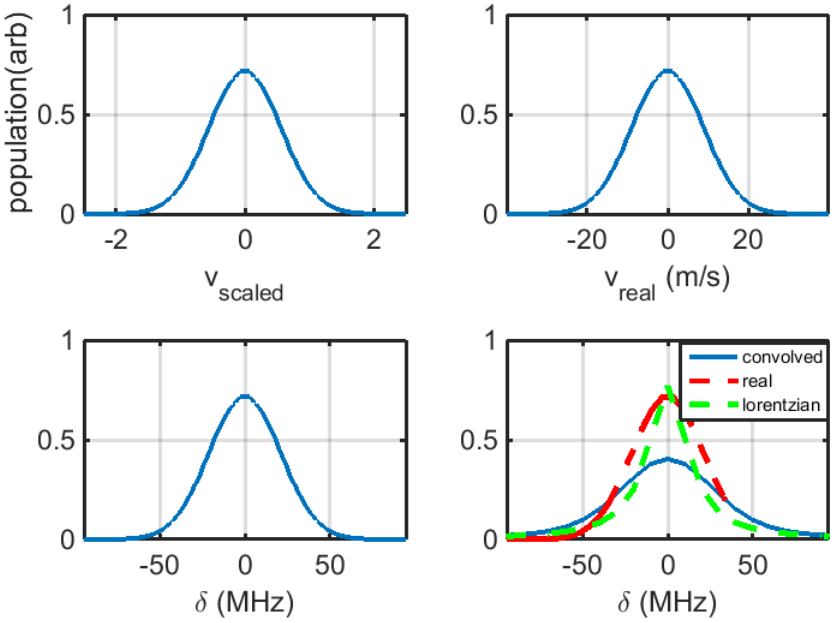

Figure 3.6 : Unscaling and convolution procedure for a given MD Distribution. Top Left: The initial scaled MD distribution. Top Right: The unscaled MD Distribution for $n = 10^{15}\mathrm{m}^{-3}$. Bottom Left: The doppler broadened MD distribution. Bottom Right: The convolved MD distribution (blue) resulting from the convolution of the doppler broadened MD distribution (red) with the imaging Lorentzian (green).

adiabatic cooling and ion heating due to electron-ion collisions, become important on that long timescale, masking the effect. [18, 23]

3.3 Experiment and Results

Using the tools and techniques discussed in Chapter 2, we acquire DIH curves over two orders of magnitude in density ($n = 3 \times 10^{14}\mathrm{m}^{-3}$ - $3 \times 10^{16}\mathrm{m}^{-3}$) and an order of magnitude in electron temperature $T_e = 50\,\mathrm{K}$ - $435\,\mathrm{K}$. This allows us to verify universality in the quench dynamics over a wide range of experimental parameters.

Figure 3.8 compares DIH curves, in both unscaled and scaled units, for {(n, T_e,

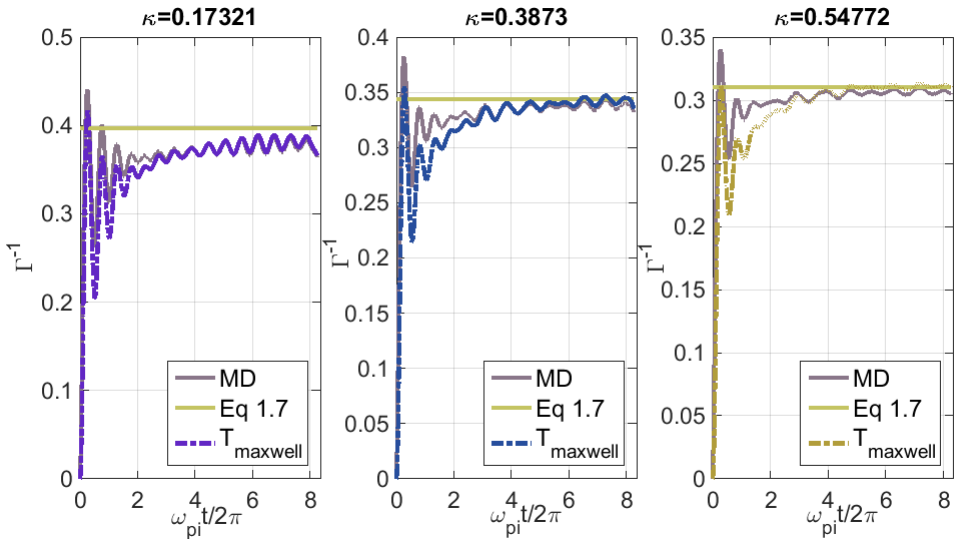

Figure 3.7 : Long timescale DIH evolution for three different κ. Γ^{-1} approaches the value predicted by Eq. 1.7, but it takes a surprisingly long time to do so. The temperature one measures when fitting a maxwellian to the MD curves (i.e. the blue distributions in Fig. 3.5) is also plotted in order to show the underestimation in energy resulting from inaccurately assuming thermalization.

$\kappa)\}$=$\{(3\times10^{14}\mathrm{m}^{-3}, 105\,\mathrm{K}, 0.23), (3\times10^{16}\mathrm{m}^{-3}, 434\,\mathrm{K}, 0.24)\}$, where the density is determined by the procedure described in Sec. 2.1.2 (these densities are later confirmed by an alternate density fitting procedure, see Ch. 4). By the universality hypothesis, the two scaled DIH curves should match each other despite the vastly different n and T_e, since their screening parameters are nearly identical. Sure enough, although there is a huge variation in the unscaled curves, the scaled curves fall right on top of each other. This is a fairly dramatic demonstration of universality in Yuakwa OCPs! This scaling is very non-trivial, as both the frequency of the oscillations and the kinetic energy each depend strongly on n and κ (see Fig. 3.4).

Next, we took two sets of data where κ was varied; one where we held $T_e = 434\,\mathrm{K}$ and adjusted n from $10^{15}\mathrm{m}^{-3}$ to $3\times10^{16}\mathrm{m}^{-3}$ (Fig. 3.9) and another where we held n relatively constant and changed T_e from $60\,\mathrm{K}$ to $434\,\mathrm{K}$ (Fig. 3.10). In both cases

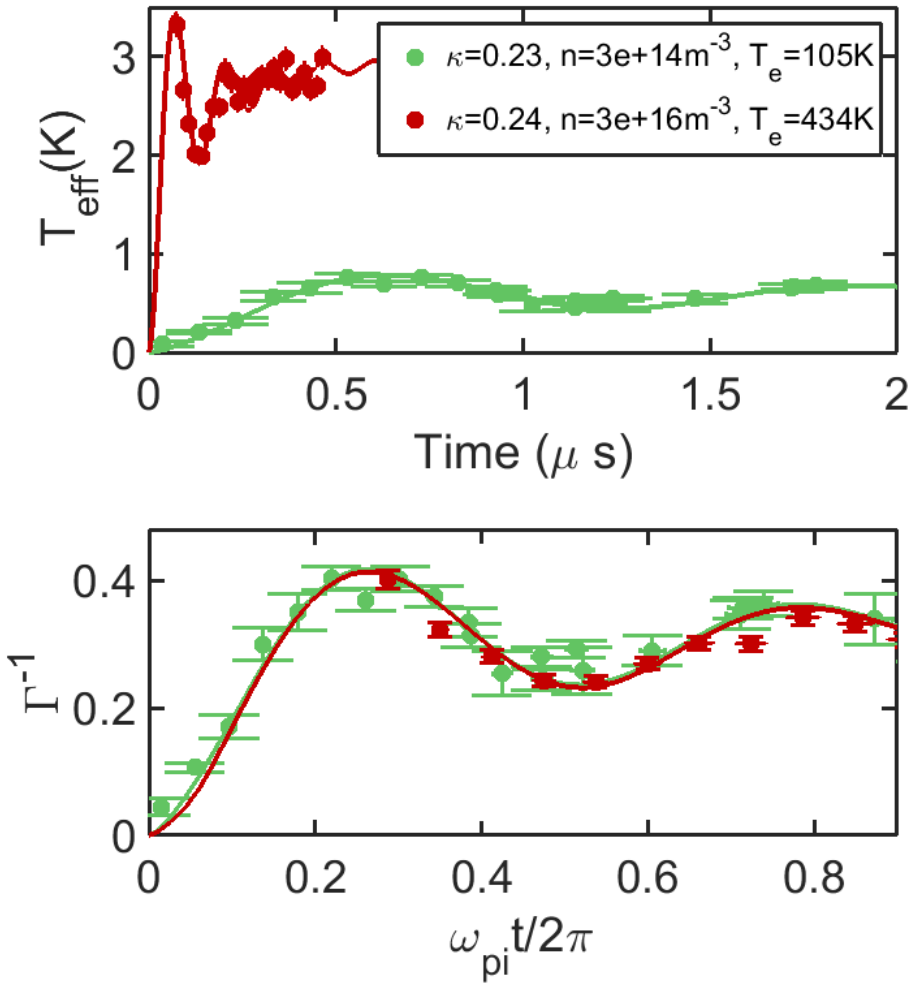

Figure 3.8 : DIH curves taken at drastically different n and T_e, but nearly identical κ. Top: DIH curves plotted in unscaled units ($T_i(t)$). Bottom: DIH curves plotted in scaled units $\Gamma^{-1}(\omega_{pi}t/2\pi)$. The lines are the temperatures from the MD data, which are determined by the process discussed in Sec. 3.2.1. Although the timescales and temperatures in the unscaled plot differ by nearly an order of magnitude, the two scaled curves are right on top of each other, matching the curve extracted from the MD simulation for κ.

we observe good qualitative agreement between the MD simulation data and the scaled experimental data; in the latter case, each experimental curve clearly falls on

a distinct κ simulation curve.

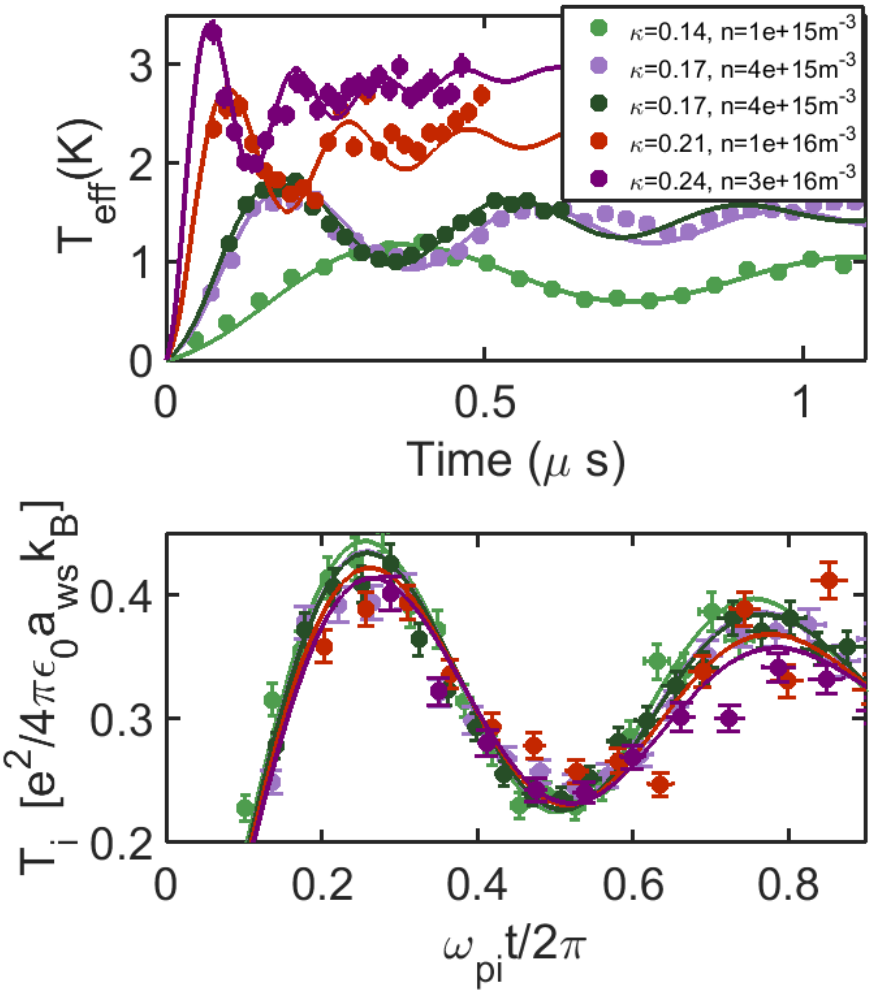

Figure 3.9 : DIH curves taken at $T_e = 434\,\mathrm{K}$, but different n, and thus different κ. Top: Unscaled data. Since the densities vary by a factor of 30, the temperature values ($T_{DIH} \propto n^{1/3}$) and oscillation timescales ($\omega_{pi} \propto \sqrt{n}$) differ for each curve. Bottom: Scaled data. Since the κ values are all relatively similar (κ has a weak dependence on n, $\kappa \propto n^{1/6}$), the scaled curves are also relatively similar.

Since the agreement was so good qualitatively, we decided to see if we could make some quantitative comparisons. We are interested in both the strength of the

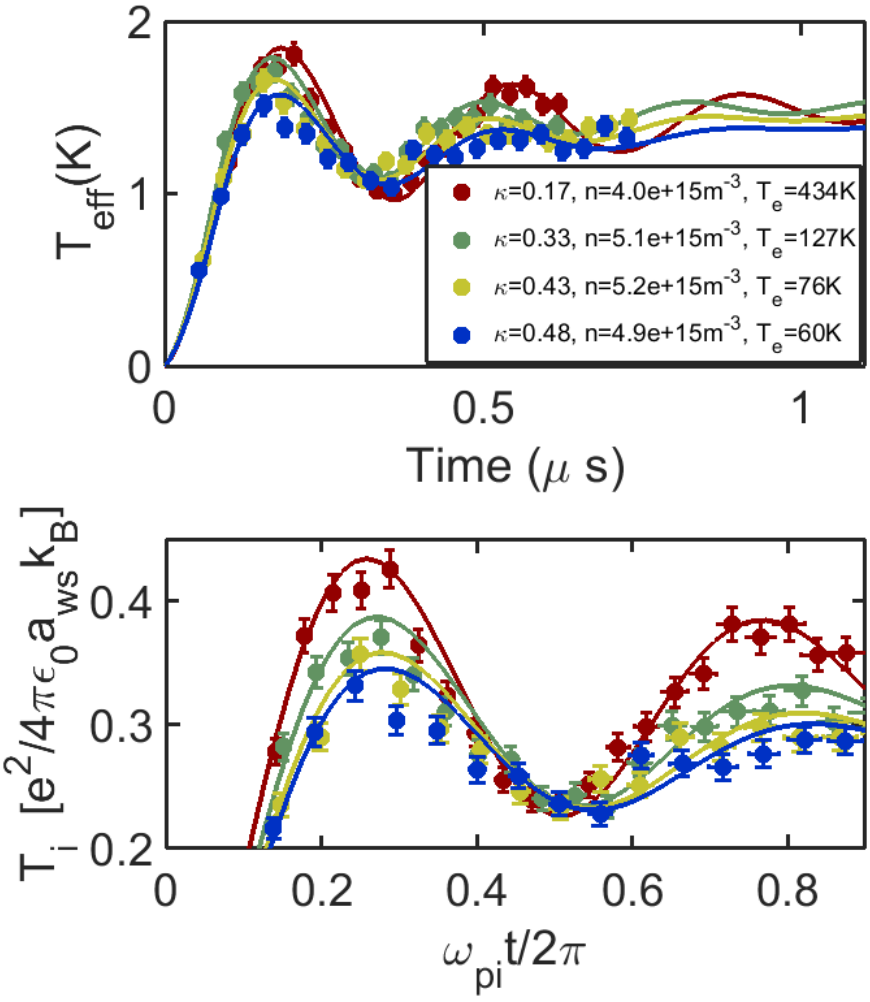

Figure 3.10 : DIH curves taken at similar n, different κ. Top: Unscaled data. Since the densities are similar, the temperature values ($T_{DIH} \propto n^{1/3}$) and oscillation timescales ($\omega_{pi} \propto \sqrt{n}$) are similar for each curve. Bottom: Scaled data. We observe remarkable qualitative agreement between the experiment and the simulation data for each screening parameter κ.

oscillations and their subsequent decay as a function of κ. In order to approach this subject, we fit the MD data in the window $0.17\omega_{pi}t/2\pi - 0.95\omega_{pi}t/2\pi$ (these limits are chosen because they provide 3 half oscillations, which we found necessary to

accurately fit both an amplitude and a decay) to a decaying sinusoidal function:

$$\Gamma^{-1}(t) = A\exp(-\gamma t)\sin(\omega t + \phi) + \Gamma_0^{-1} \tag{3.2}$$

where A, γ, ω, ϕ, and Γ_0 are all fit parameters. The frequency falls with κ (Fig. 3.11), as observed in the BYU experiment. [2]

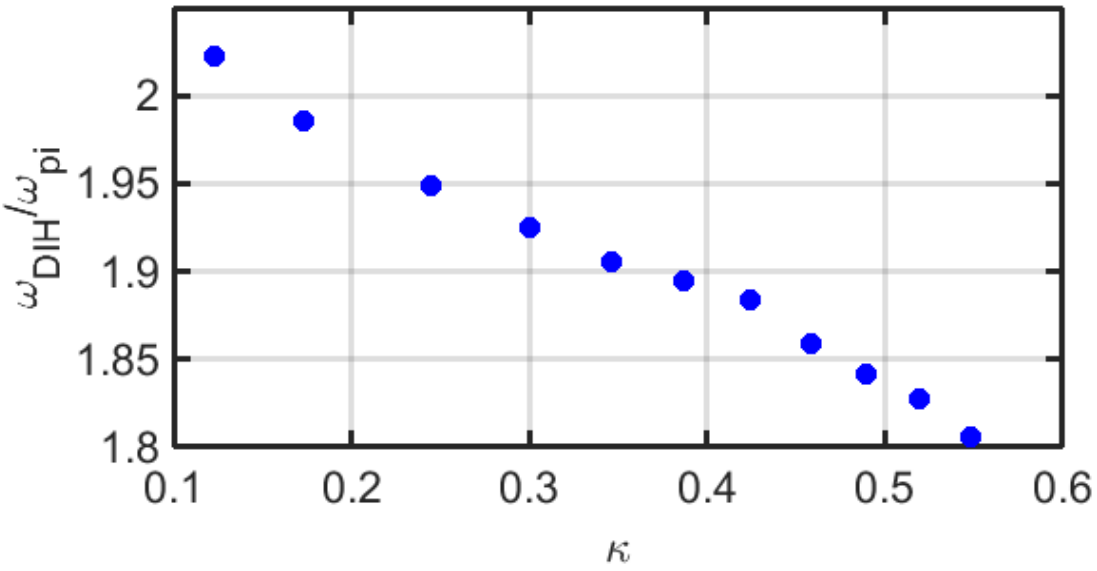

Figure 3.11 : $\omega_{DIH}(\kappa)/\omega_{pi}$ determined by fitting the MD data from $\omega_{pi}t/2\pi = 0.17$ to $\omega_{pi}t/2\pi = 0.95$.

We then fit the experimental data in that same window to Eq. 3.2. However, we found that we needed to fix the frequency to the frequency measured from the fits to the MD curves, $\omega(\kappa)$ (Fig. 3.11), in order to better constrain the fits to yield accurate measures of the amplitude and the decay (A and γ, respectively) of the oscillations. Our results of these fits, along with a comparison to the values extracted from the fits to the MD data, are shown in Figure 3.12; we observe good agreement between the experiment and the simulation.

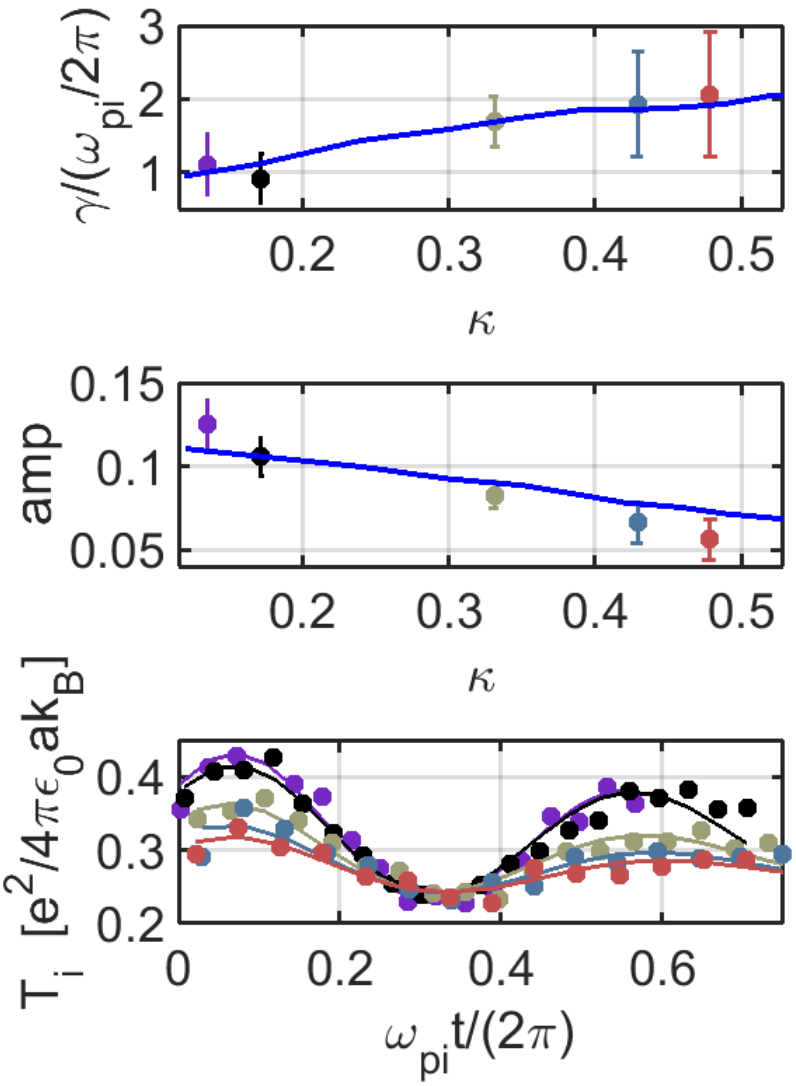

Figure 3.12 : Top: $\gamma(\kappa)/(\omega_{pi}/2\pi)$, Middle: $A(\kappa)$, Bottom: DIH curve data along with the corresponding fit to Eq 3.2. Error bars indicate $\pm 1\sigma$ uncertainty in the fitting values. We clearly observe, both from the fits to the simulation and to the experiment, that the oscillations both start out weaker and decay faster as κ increases.

However, by comparing our data directly to the MD data, we have implicitly ignored density variations, both known and unknown, in the experiment. Averaging

together different DIH curves corresponding to different densities will increase the observed decay rate, as the different curves will dephase due to the density dependence of the frequency. We now turn to a discussion of these effects.

3.3.1 Effect of Density Averaging

Density fluctuations manifest in two ways in our experiment. First, each plasma "image" (ex: Fig. 2.5) is actually a compilation of LIF images of $\sim$ 1000 plasmas. Ideally, all of these plasmas would have the same size, density, electron temperature, etc. However, there is some natural shot to shot fluctuation in all of these parameters. We believe our shot to shot density distribution to be a normal distribution with a standard deviation somewhere between 10% and 20% of the mean density. Second, our plasmas inherit the gaussian spatial distribution of the MOT, i.e., they have non uniform density. We look at temperature data from a $1\sigma \times 1\sigma$ region around the center of the plasma (see Chapter 2). The fluctuations in density within this region, in addition to the unresolvable fluctuations along the 1 mm slit, form another source of density fluctuations.

Since the frequency of the KEOs depends on density through ω_{pi}, averaging in different density components results in damping of the KEOs through dephasing. Fig. 3.13 shows how the dephasing due to the different types of density fluctuations affects the predicted MD DIH curves. Clearly, our main source of density fluctuation dependent dephasing is due to the shot to shot fluctuations, which unfortunately we currently have no control over. The dephasing becomes quite pronounced after a couple of oscillations, which is why we restricted the fits in the previous section to the window $\omega_{pi}t/2\pi = 0.17$ to $\omega_{pi}t/2\pi = 0.95$.

Therefore, in order to accurately compare our experimental results to the MD re-

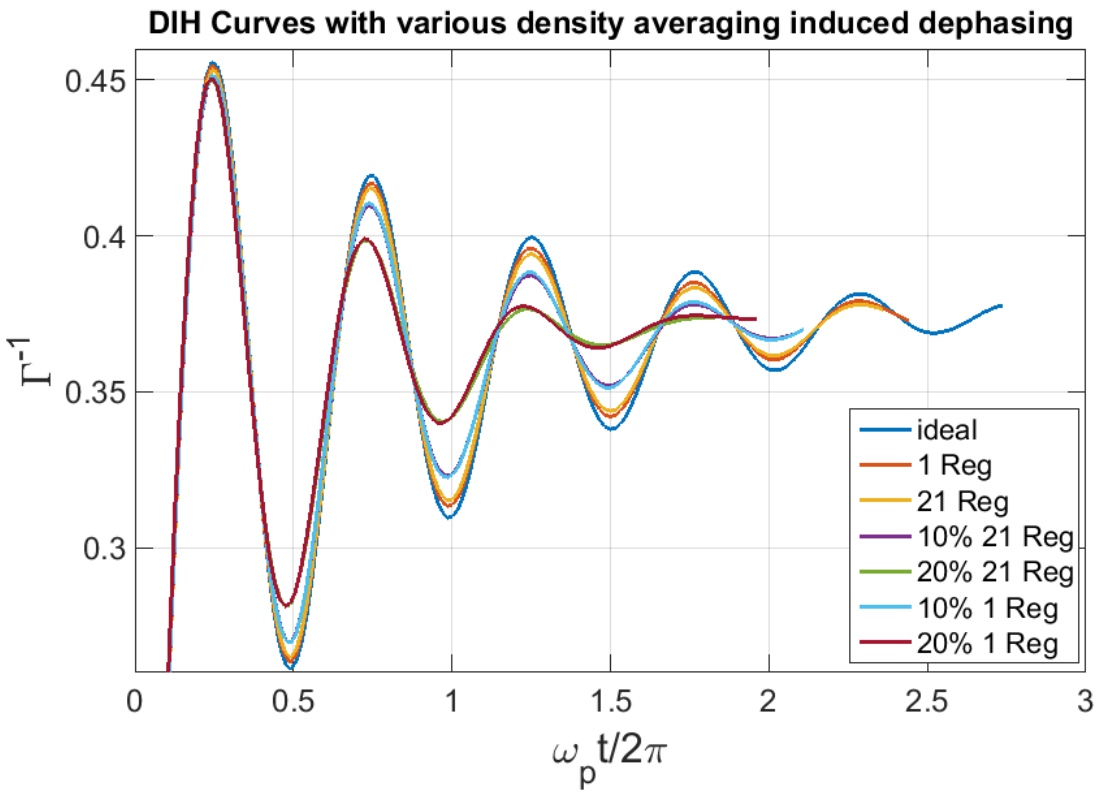

Figure 3.13 : Effect of Density averaging on DIH curves for $\kappa = 0.12$. "1 Reg" refers to a DIH curve where the only density variations considered are due to the slit and the averaging along the y-axis of the image perpendicular to the imaging beam axis. "21 Reg" includes the averaging from considering multiple regions along the imaging beam axis. The percentages refer to the standard deviation of the shot to shot density distribution, which is assumed to be normal (0% unless indicated otherwise). The shot to shot fluctuations clearly dominate the dephasing, and become very effective at 20% after just one oscillation. This is why we focus only on the first oscillation and a half in our analysis.

sults, we must factor in these density fluctuations. We do so by fitting the theoretical, density fluctuation dependent, MD curves to a decaying sinusoid in the same time window in which we fit our data. Since the magnitude of the shot to shot density fluctuations is unknown, while the averaging over regions is always constant, we fit the MD data corresponding to 0%, 10%, and 20% density fluctuations, in each case

averaging over the 21 regions (i.e., the yellow, purple, and green curves in Fig. 3.13). The results are displayed in Figure 3.14. The trend in the variation of amplitude and damping with kappa matches between theory and experiment. Given the good agreement overall between numerical simulation and the data for describing KEOs and DIH, we interpret Figure. 3.14 as placing an upper limit on our shot-to-shot density fluctuations at about 10%.

3.4 Future Work

Figures 3.8 and 3.10 show that we have achieved our goal of demonstrating universality in the post photoionization quench from $\kappa_0 = \infty$ to κ. However, we still have a mystery: what is the connection between the equilibration process (DIH) and collective modes (KEOs)? Clearly, these oscillations have a strong dependence on κ, as shown in Figure. 3.12. Perhaps this is a clue pointing us towards the source of the KEOs?

Indeed, a conceptual picture where the KEOs emerge from the ions overshooting their equilibrium positions during the initial propulsion away from their nearest neighbors, has some allure. In this picture, one would expect the oscillations to weaken with κ, as the electrons become more effective at screening the ion-ion interactions which lead to the initial overshoot and subsequent pull-back. We intend to further examine the underlying MD data in order to determine attributes of the KEOs, such as their mode structure in k-space, and see whether or not they can provide further clues towards the source of these oscillations, which are ubiquitous in plasma equilibration phenomena. [38, 26, 30, 28, 5, 2]. We will also further explore why it is that the oscillations damp more rapidly as screening increases.

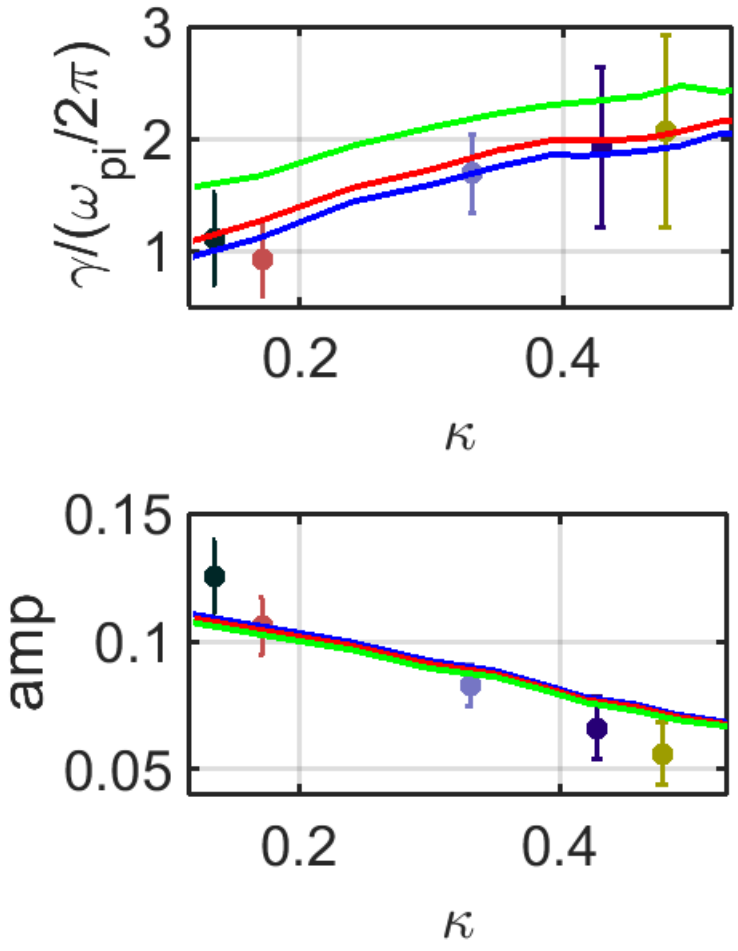

Figure 3.14 : Blue: fit to MD curve with 0% standard deviation in density, Red: 10%, Green: 20%. Error bars indicate $\pm 1\sigma$ uncertainty in the fitting values. The data is still a reasonable match to the curves, as it was in Fig. 3.12, but the additional uncertainty makes it more difficult to make quantitative comparisons.

Chapter 4

Using Universality as a precision probe of UNP Density

In the previous chapter, we demonstrated the universality of DIH with respect to κ over a wide range of n and T_e when temperatures and times are scaled appropriately. In this chapter, we demonstrate how universality can be inverted to measure n given a known κ and a DIH curve. We will also compare and contrast this method of measuring n to the method discussed in Chapter 2, which used the frequency-integrated LIF signal to determine n.

4.1 Method

We observed in the previous chapter that there is a 1:1 correspondence between κ and a DIH curve when T and t are scaled to $\Gamma^{-1} = (k_B/(e^2/4\pi\epsilon_0 a))T$ and $\omega_{pi}t$, respectively. Both of the scaling factors depend solely on n. Thus, given a known T_e and an experimental DIH curve in unscaled units ($T(t)$), one can use the following iterative fitting process to determine n:

- Pick an initial n. From this n and the known T_e, calculate κ.
- Interpolate over the MD library (Fig. 3.4) to determine the corresponding scaled DIH curve for κ.
- Scale the experimental DIH curve using the n dependent scaling factors.

- Compare this scaled curve to the MD curve
- Pick a new n and repeat steps 1-4 until the solution converges to the density of best fit, n_{fit}.

There are many scientific computing tools which can implement these sorts of methods. We opted to use Matlab's "nlinfit" function to perform a non-linear regression on the $T(t)$ curve with T_e and the imaging parameters (γ_L, s_0) as known parameters (the former is needed to calculate κ and the latter two are needed for the numerical convolution of the MD data discussed in Sec. 3.2.1) and n as the only free parameter. The model "function" used in the regression is simply $\Gamma_{MD}^{-1}(\kappa, \omega_{pi}t)$, the MD library.

Let's compare this method of determining n (this will be referred to as the "DIH method") to the method discussed in Ch. 2, in which we fit the frequency-integrated LIF signal to Eq. 2.7 (this will be referred to as the "camera method"). Utilization of the camera method requires knowledge of a lot of parameters:

- $C = f_{capt}C_{P\to S}$, where f_{capt} is the fraction of emitted photons captured by the camera and $C_{P\to S}$ is the photon to signal conversion factor. In practice, this overall calibration factor is determined by calibrating LIF images either to plasma absorption images or to loss from the MOT [3].
- s_0, the saturation parameter at the center of the beam
- w_y, the width of the laser beam along the y-axis (the axis perpendicular to both the slit and the camera axis).
- d, the slit size

If our knowledge of any of these 5 parameters (f_{capt}, $C_{P\to s}$, s_0, w_y, d) is inaccurate, we will mis-measure n. Moreover, there are some situations in which the fit to Eq. 2.7 fails. For example, we have difficulty fitting when the size of the plasma is comparable to the field of view.

The DIH method, in contrast, has no dependence on most of these experimental parameters (the temperature weakly depends on s_0 and γ_L through the numerical convolution of the MD Data and the convolution of the Doppler broadened width of the real data). It is much less sensitive to, for example, misalignment of the imaging beam on the plasma, or on degradation of the camera over time, than the camera method is.

4.2 Results

Figure 4.1 shows typical results from fitting DIH curves for n over a range of n and T_e. The data fits remarkably well (compare the curve of best fit to the curves of $\pm 10\%$ uncertainty) for high T_e (all but the bottom right plot in Fig. 4.1). In this region, the non-linear regression determined that the 95% confidence interval corresponded to a typical density uncertainty of $\sim 5\%$. At low T_e (i.e., high κ), qualitatively the fit is less impressive: the temperature data, at times, significantly undershoots the curve of best fit.

The next step was to compare the DIH method to the camera method. In principle, they should yield the same density measurements assuming that we've measured all the parameters which go into the camera method correctly. Fig. 4.2 plots the ratio of the two density measurements, n_{fit}/n_{camera} where n_{fit} is measured using the DIH method and n_{camera} is the density measured using the camera method, vs κ for a wide range of plasma densities. The two agree very well (i.e., the ratio is pretty

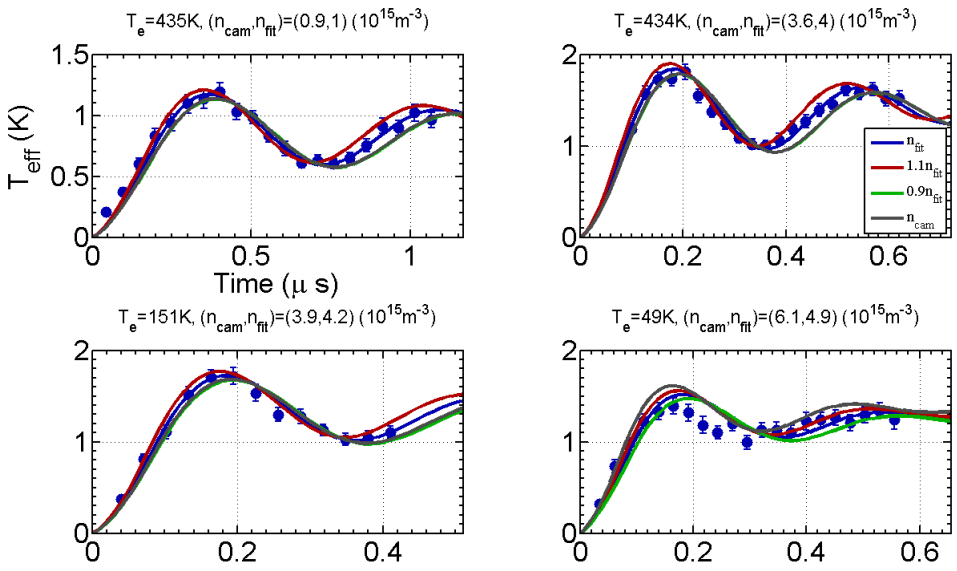

Figure 4.1 : Typical results from fitting DIH curves for n using the MD library. In all but the bottom right plot, the data matches the curve of best fit very well compared to the curves corresponding to $\pm 10\%$ variations in n (the red and green curves). The gray curve corresponds to the MD curve corresponding to the density measured by the camera method. In the bottom right plot, we observe that the density fit does not seem to work very well. We attribute this to non-Yukawa OCP physics, such as three body recombination

constant with respect to κ, and is near unity) up to $\kappa > 0.4$, at which point n_{fit} starts to drop relative to n_{camera}. In the bottom right DIH curve in Fig. 4.1, this manifested in temperature measurements which correspond to a density much lower than that measured by the camera method. In other words, either the camera is somehow artificially observing a higher density, something is cooling the plasmas, or our measurement of κ is off somehow, which would cause DIH to be fit incorrectly.

We considered a couple of possible sources of this discrepancy between the methods:

- *Charge Exchanging collisions with ground state atoms*: One possible reason

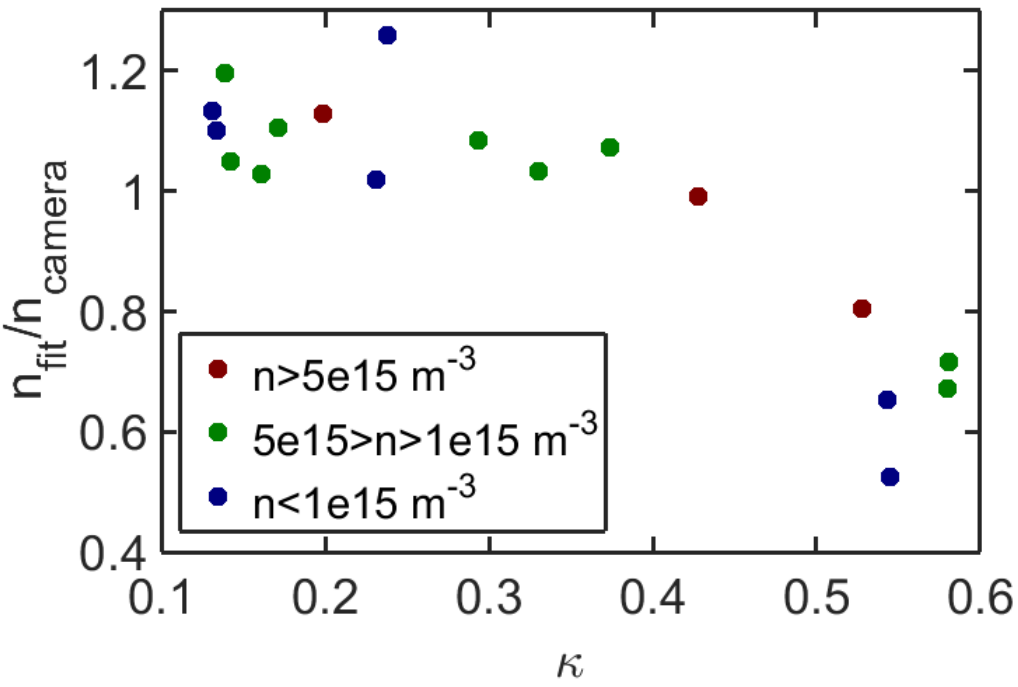

Figure 4.2 : n_{fit}/n_{camera} vs κ.

why colder temperatures would be observed is the presence of charge exchange collisions between hot ions and cold ground state atoms. Population swapping between ions and neutrals would make the ions colder. However, this seems unlikely: the typical cross section for such collisions is $\sigma_{cEx} \sim 10^{-19}\mathrm{m}^{-2}$. This would give a mean free path of $1/n\sigma_{cEx} = 1640$ meters for a ground state density of $n = 6 \times 10^{15}\mathrm{m}^{-3}$. As this is orders of magnitudes larger than the plasma size, we can safely discount this possibility.

- *Charge Exchanging collisions with rydberg atoms*: The cross section for charge exchange interactions scales as n_q^4, where n_q is the principle quantum number. Thus, if there were a large amount of cold rydberg atoms, the charge exchange

collisions could be effective: for $n_q = 100$, the mean free path is $1/n\sigma_{cEx} = 16\mu\,\mathrm{m}$ for $n = 6 \times 10^{15}\mathrm{m}^{-3}$.

However, the density of rydberg atoms is not nearly that high. Rydberg atoms are generated in a UNP through a three body recombination process where two electrons and an ion collide to form one rydberg atom and one electron which carries the binding energy of the rydberg atom. The rate of TBR events was determined by Mansbach and Keck using Monte Carlo simulations [20]

$$R_{TBR}(s^{-1}) = 4.5 \times 10^{-21} T_e^{-9/2} \int n_e^2(r) n_i(r) 4\pi r^2 dr \tag{4.1}$$

Applying this equation for the parameters in the bottom right plot in Fig. 4.1 over a sphere with radius $\sigma/2$ centered at the center of the plasma gives a total rydberg density in that region of $n_r \sim 4 \times 10^{12}\mathrm{m}^{-3}$ after 170 ns (the time of the DIH peak). Calculating the mean free path using this density and $\sigma_{cEx} = 10^{-11}\mathrm{m}^{-2}$ yields $1/n\sigma_{cEx} = 25\,\mathrm{mm}$, which is still an order of magnitude larger than the size of the cloud. So, we can also rule out this possibility.

- *Uncertainty in the camera measurement*: Rydberg atoms which have undergone l-changing collisions become visible using the LIF transition due to their core electron [24]. Thus, if there were a large amount of rydberg atoms, the camera would measure an artificially high plasma density, as we would also mistakenly be including rydberg atoms, which would explain our observations. However, we've already determined that the rydberg density is around 0.1% of the plasma density, making this an unlikely source of error.

- *Other TBR Effects*: TBR also heats the electrons, which would result in additional changes in κ beyond the original quenching to κ_f. The constantly

changing κ would have unpredictable effects on the DIH curve. We cannot discount this possibility, however, the Rice group previously determined that TBR does not heat the electrons much for $\kappa < 0.55$ [11], whereas differences in density measurements are observed at $\kappa \sim 0.4$.

- *Uncertainty in* κ: The wavelength of the ionization beam, and thus the electron temperature, is controlled by a grating. We do not continuously monitor the frequency. It is possible that the calibration to the grating is off, which would mean that we are not fitting the DIH curve corresponding to the actual κ of the plasma. This effect would become more significant as the electron temperatures get lower, which coincide with higher κ, which is where we observe the difference between the two density measurements. It is also possible that there is some amplified spontaneous emission (ASE) in the beam; the wavelength of ASE light is not controlled by the grating, and therefore would change the electron temperature.

Although we have not yet confirmed what exactly the source of the error is, all of the explanations listed above point towards any errors being largely confined to the low T_e (high κ) regime. Outside of this regime (e.g. $\kappa < 0.4$), errors are minimized, and we observe a constant 10% difference between the two density measurements. We attribute this to an error in the camera calibration, as the density fits to DIH are nearly perfect in this regime (all plots other than the bottom right in Fig. 4.1).

Chapter 5

Conclusion

In this thesis we've studied the dynamics of a rapid quench from a non-interacting gas to a Yukawa OCP with a controllable screening parameter κ_f. In particular, we looked at the evolution of the ion kinetic energy vs time after the photoionization of an uncorrelated $\sim 10\,\mathrm{mK}$ atomic gas. We've done this using UNPs, which are a nearly ideal realization of Yukawa OCPs, as they contain only one positive charge species ($Z = 1$) which is much heavier, and thus slower, than the electrons within the plasma, and they are clearly in the classical plasma regime. We have confirmed that the quench dynamics are universal in κ_f when kinetic energy and time are scaled by $e^2/(4\pi\epsilon_0 a)$ and $2\pi/\omega_{pi}$, respectively.

This is a specific example of the general phenomena of universality in a Yukawa OCP; all dynamics should depend only on κ when the plasma quantities are scaled appropriately. This powerful tool is what allows plasma researchers to study plasmas of dramatically different densities and temperatures using the same framework, allowing UNP physics to successfully provide a window into the physics of astrophysical plasmas and the plasmas produced in inertial confinement fusion experiments. In our studies of DIH, we varied densities over two orders of magnitude (n from $3 \times 10^{14}\mathrm{m}^{-3}$ to $3 \times 10^{16}\mathrm{m}^{-3}$) and electron temperatures over an order of magnitude (T_e from $49\,\mathrm{K}$ to $434\,\mathrm{K}$) and confirmed that all DIH curves collapsed onto the appropriate universal κ_f dependent curve taken from MD simulations. We demonstrated one application of the universal scaling features by inverting them in order to measure the density of

a plasma with a known T_e given a DIH curve.

Having determined that the KEOs observed during DIH are a universal, κ dependent, feature, future work will focus on determining the connection between the equilibration process and collective modes, which manifests in the KEOs. In particular, why does increasing κ both reduce the magnitude of the collective behavior and make it damp more rapidly? Answering these questions will provide more insight into the general aspects of how collective mode coupling manifests in all strongly coupled plasma systems.

Appendices

Appendix A

Derivation of $g(r)$ and related quantities

For a given model pair-wise potential (e.g. the Yukawa potential for a Yukawa OCP) $v(r_{ij})$, the effect of the interactions is best accounted for by considering their effect on the pair distribution function, which is defined as [13]:

$$g^{(2)}(\vec{r}_1, \vec{r}_2) = V^2 P_N^{(2)}(\vec{r}_1, \vec{r}_2) \tag{A.1}$$

in terms of the conditional probability function $P^{(2)}$

$$P_N^{(2)}(\vec{r}_1, \vec{r}_2) = \int ... \int P_N^N(\vec{r}_1, ...\vec{r}_N) d\vec{r}_3 ... d\vec{r}_N \tag{A.2}$$

which describes the probability density for two particles to be located at fixed points $\vec{r}_1$ and $\vec{r}_2$ while all other particles positions are allowed to vary. This, in turn, is expressed in terms of the total probability density

$$P_N^N(\vec{r}_1, ...\vec{r}_N) = \frac{1}{Z_N} \exp[-\beta v_N(\vec{r}_1, ...\vec{r}_N)] \tag{A.3}$$

where Z_N is the partition function ($Z_N = \int ... \int \exp[-\beta v_N(\vec{r}_1, ...\vec{r}_N)] d\vec{r}_1 ... d\vec{r}_N$) and $v_N(\vec{r}_1, ...\vec{r}_N) = \sum_{i<j} v(r_{ij})$ is the total interaction energy of the system given particle coordinates $\{\vec{r}_1 ... \vec{r}_N\}$. This is interpreted as the probability of simultaneously finding particle 1 at r_1, particle 2 at r_2, etc.

In a homogeneous mixture with pair interactions, all dependence on $\vec{r}_1$ and $\vec{r}_2$ comes from the distance $r = |\vec{r}_1 - \vec{r}_2|$. So, I'll write $g^{(2)}(\vec{r}_1, \vec{r}_2) = g(r)$. $g(r)$ simply

reflects how local density near any given particle (taken to be at the origin) is modified by the correlations: $n_{local}(r) = g(r)n$. For example, in the non-interacting limit ($v_N = 0$) we have $Z_N = V^N$, from which we can obtain $P_N^{(2)}(r) = V^{-2}$, and $g(r) = 1$.

Evaluating $g(r)$ requires deciding on a form for $v(r_{ij})$, such as the Yukawa interaction. Even after deciding on that form, $g(r)$ is often difficult to calculate, as it is coupled to higher-order correlators ($g^{(3)}(r_{ij}, r_{ik}, r_{jk})$, etc.) via the "Yvon-Born-Green" (YGB) hierarchy, which is similar to the BBGYK hierarchy for the conditional probability densities. Cutting off the hierarchy becomes difficult in strongly coupled systems, so we must typically resort to simulations by methods such as Molecular Dynamics (MD) to determine $g(r)$, as discussed in Section 1.3.

However, once $g(r)$ is determined, all other equilibrium thermodynamic properties of the system can be derived from it. For example, consider the total energy of the system. For a non-interacting gas, $U_i = \frac{3}{2}Nk_BT$. For an interacting gas there are also contributions to the total internal energy stemming from the interactions. The total energy can thus be written $U = U_i + U_{exc}$ where:

$$U_{exc} = \frac{1}{Z_N} \int \exp[-\beta v_N(\vec{r}_1, ...\vec{r}_N)] v_N(\vec{r}_1, ...\vec{r}_N) d\vec{r}_N \tag{A.4}$$

Dividing by N, U_{exc} can be rewritten [13]

$$\frac{U_{ex}}{N} = \frac{1}{NZ_N}\int \exp[-\beta v_N(r_N)] \sum_{i\neq j} v(r_{ij}) d\vec{r}_N \tag{A.5}$$

$$= \frac{1}{NV^2}\int\int \frac{N^2}{2} v(r_{12}) \left(\frac{V^2}{Z_N}\int ... \int \exp[-\beta V_N(r_N)] d\vec{r}_3 ... d\vec{r}_N\right) d\vec{r}_1 d\vec{r}_2 \tag{A.6}$$

$$= \frac{N}{2V^2}\int\int v(r_{12}) g(\vec{r}_1, \vec{r}_2) d\vec{r}_1 d\vec{r}_2 \tag{A.7}$$

$$= \frac{N}{2V^2}\int\int v(r_{12}) g(\vec{r}_{12}) d\vec{r}_1 d\vec{r}_{12} \tag{A.8}$$

$$= \frac{N}{2V}\int v(r_{12}) g(\vec{r}_{12}) d\vec{r}_{12} \tag{A.9}$$

$$= 2\pi n \int_0^\infty g(r) v(r) r^2 dr \tag{A.10}$$

$$= \frac{3}{2}\int_0^\infty g(\tilde{r}) v(\tilde{r}) \tilde{r}^2 d\tilde{r} \tag{A.11}$$

where I've defined $\tilde{r} = r/a$, and $a = \left(\frac{3}{4\pi n}\right)^{1/3}$ is the average interparticle spacing (note: this is the derivation supporting Eq. 1.5 in Chapter 1). Similar expressions can be found for quantities like the equation of state and the Helmholtz free energy.

For the Yukawa model for describing one-component plasmas (OCP), $v(\tilde{r}_{ij})$ takes the form:

$$v(\tilde{r}_{ij}) = \frac{(Ze)^2}{4\pi\epsilon_0 a}\frac{\exp[-\kappa\tilde{r}]}{\tilde{r}} \tag{A.12}$$

and therefore:

$$\beta v(\tilde{r}_{ij}) = \frac{v(\tilde{r}_{ij})}{k_B T} = \Gamma\frac{\exp\left[-\kappa\tilde{r}_{12}\right]}{\tilde{r}_{12}} \tag{A.13}$$

where $\Gamma = \frac{(Ze)^2/4\pi\epsilon_0 a}{k_B T}$, the "Coulomb Coupling parameter", is the per-particle ratio of interaction energy to kinetic energy, and $\kappa = a/\lambda_D$ is the "screening parameter".

We can then rewrite $g(r)$ for the ions as

$$g_{ii}(\tilde{r},\Gamma,\kappa) = \exp\left[-\Gamma\frac{\exp[-\kappa\tilde{r}]}{\tilde{r}}\right]\frac{\int_{V'}\cdots\int_{V'}\exp\left[-\Gamma\sum_{i>2,i>j}\frac{\exp[-\kappa\tilde{r}_{ij}]}{\tilde{r}_{ij}}\right]d\vec{\tilde{r}}_3...d\vec{\tilde{r}}_N}{\int_{V'}\cdots\int_{V'}\exp\left[-\Gamma\sum_{i>j}\frac{\exp[-\kappa\tilde{r}_{ij}]}{\tilde{r}_{ij}}\right]d\vec{\tilde{r}}_1...d\vec{\tilde{r}}_N} \tag{A.14}$$

where $V' = \frac{4}{3}\pi N$. In the term in the denominator (the partition function) we integrate over all possible positions of all the ions while in the term in the numerator we allow all particles *except* the two fixed at $\vec{r}_1$ and $\vec{r}_2$ to vary and integrate over all those allowed positions. This allows us to remove the $\exp\left[-\Gamma\frac{\exp[-\kappa\tilde{r}]}{\tilde{r}}\right]$ term from the integration. We still must leave in terms like r_{31}, r_{32}, r_{N1}, etc. in the integration in the numerator as $\vec{r}_3...\vec{r}_N$ are allowed to vary.

When g_{ii} is written in this way, it is clear that it depends only on Γ and κ as claimed in the thesis. Therefore, all thermodynamic properties of the system also depend solely on Γ and κ, as they can be derived immediately from $g(r)$, as was explicitly demonstrated for U_{exc} in Eq. A.11.

Bibliography

[1] G. Bannasch, J. Castro, P. McQuillen, T. Pohl, and T. C. Killian. Velocity relaxation in a strongly coupled plasma. *Phys. Rev. Lett.*, 109:185008, 2012.

[2] S. D. Bergeson, A. Denning, M. Lyon, and F. Robicheaux. Density and temperature scaling of disorder-induced heating in ultracold plasmas. *Phys. Rev. A.*, 83:023409, 2011.

[3] J. Castro. *Collective effects in Ultracold Neutral Plasmas.* PhD thesis, Rice University, 2011.

[4] J. Castro, P. McQuillen, and T.C. Killian. Ion acoustic waves in ultracold neutral plasmas. *Phys. Rev. Lett.*, 105:065004, 2010.

[5] Y. C. Chen, C. E. Simien, S. Laha, P. Gupta, Y. N. Martinez, P. G. Mickelson, S. B. Nagel, and T. C. Killian. Electron screening and kinetic-energy oscillations in a strongly coupled plasma. *Phys. Rev. Lett.*, 93:265003, 2004.

[6] M. Robert de Saint-Vincent, C. S. Hofmann, H. Schempp, G. Gunter, S. Whitlock, and M. Weidemuller. Spontaneous avalanche ionization of a strongly blockaded rydberg gas. *Phys. Rev. Lett.*, 110:045004, 2013.

[7] Z. Donko, P. Hartmann, and G.J. Kalman. Strongly coupled plasma liquids. *Arxiv: http://arxiv.org/pdf/0710.5229.pdf.*

[8] D O Gericke, M S Murillo, D Semkat, M Bonitz, and D Kremp. Relaxation of strongly coupled coulomb systems after rapid changes of the interaction potential. *J. Phys. A*, 36:6087, 2003.

[9] D.O. Gericke and M.S. Murillo. Disorder-induced heating of ultracold plasmas. *Contrib. Plasma Phys*, 43:298, 2003.

[10] H. Gould and G.F. Mazenko. Coupling of single-particle and collective motions in a one-component plasma. *Phys. Rev. Lett.*, 35:1455, 1975.

[11] P. Gupta, S. Laha, C. E. Simien, H. Gao, J. Castro, T. C. Killian, and T. Pohl. Electron-temperature evolution in expanding ultracold neutral plasmas. *Phys. Rev. Lett.*, 99:155001, 2007.

[12] S. Hamaguchi, R. T. Farouki, and D. H. E. Dubin. Triple point of yukawa systems. *Phys. Rev. E.*, 56:4671, 1997.

[13] J.P. Hansen and I.R. McDonald. *Theory of Simple Liquids*. Academic Press Inc. (London), 1976.

[14] J.P. Hansen, E.L. Pollock, and I.R. McDonald. Velocity autocorrelation function and dynamical structure factor of the classical one-component plasma. *Phys. Rev. Lett.*, 32:6, 1974.

[15] T. C. Killian. Ultracold neutral plasmas. *Science*, 316:705, 2007.

[16] T. C. Killian, S. Kulin, S. D. Bergeson, L. A. Orozco, C. Orzel, and S. L. Rolston. Creation of an ultracold neutral plasma. *Phys. Rev. Lett.*, 83:23, 1999.

[17] S. Laha, Y. C. Chen, P. Gupta, C. E. Simien, Y. N. Martinez, P. G. Mickelson,

S. B. Nagel, and T. C. Killian. Kinetic energy oscillations in annular regions of ultracold neutral plasmas. *Eur. Phys J. D*, 40:51, 2006.

[18] S. Laha, P. Gupta, C. E. Simien, H. Gao, J. Castro, and T. C. Killian. Experimental realization of an exact solution to the vlasov equations for an expanding plasma. *Phys. Rev. Lett.*, 99:155001, 2007.

[19] M Lyon and S. D Bergeson. The influence of electron screening on disorder-induced heating. *J. Phys. B*, 44:184014, 2011.

[20] P. Mansbach and J. Keck. Monte carlo trajectory calculations of atomic excitation and ionization by thermal electrons. *Phys. Rev.*, 181:275, 1969.

[21] B.R. Martin and G.P. Shaw. *Particle Physics*. Manchester Physics Series. Wiley, 2008.

[22] J.M. Maxson, I.V. Bazarov, W. Wan, H.A. Padmore, and C.E. Coleman-Smith. Fundamental photoemission brightness limit from disorder induced heating. 15:103024, 2013.

[23] P. McQuillen, T. Strickler, T. Langin, and T. C. Killian. Ion temperature evolution in an ultracold neutral plasma. *Physics of Plasmas*, 22:033513, 2015.

[24] P. McQuillen, X. Zhang, T. Strickler, F.B. Dunning, and T.C. Killian. Imaging the evolution of an ultracold strontium rydberg gas. *Phys. Rev. A.*, 87:013407, 2013.

[25] K. Morawetz, M. Bonitz, V. G. Morozov, G. Röpke, and D. Kremp. Short-time dynamics with initial correlations. *Phys. Rev. Lett.*, 35:21, 1975.

[26] I V Morozov and G E Norman. Non-exponential dynamic relaxation in strongly nonequilibrium nonideal plasmas. *J. Phys. A*, 36:6005, 2003.

[27] J. P. Morrison, C. J. Rennick, J. S. Keller, and E. R. Grant. Evolution from a molecular rydberg gas to an ultracold plasma in a seeded supersonic expansion of no. *Phys. Rev. Lett.*, 101:205005, 2008.

[28] Michael S. Murillo. Ultrafast dynamics of neutral, ultracold plasmas. *Physics of Plasmas*, 14:055702, 2007.

[29] M.S. Murillo. Using fermi statistics to create strongly coupled ion plasmas in atom traps. *Phys. Rev. Lett.*, 87:115003, 2001.

[30] M.S. Murillo. Ultrafast dynamics of strongly coupled plasmas. *Phys. Rev. Lett.*, 96:165001, 2006.

[31] T. Pohl, T. Pattard, and J. M. Rost. Coulomb crystallization in expanding laser-cooled neutral plasmas. *Phys. Rev. Lett.*, 92:155003, 2004.

[32] T Pohl, T Pattard, and J M Rost. On the possibility of 'correlation cooling' of ultracold neutral plasmas. *J. Phys. B*, 37:183, 2004.

[33] M. P. Robinson, B. L. Tolra, M. W. Noel, T. F. Gallagher, and P. Pillet. Spontaneous evolution of rydberg atoms into an ultracold plasma. *Phys. Rev. Lett.*, 85:4466, 2000.

[34] S. L. Rolston, S. D. Bergeson, S. Kulin, and C. Orzel. A strongly coupled plasma or a dense rydberg gas? 43:1324, 1998.

[35] J.E. Sansonetti. Wavelengths, transition probabilities, and energy levels for the

spectra of strontium ions (sr ii through sr xxxviii). *J. Phys. Chem. Ref. Data.*, 41:013102, 2012.

[36] C. E. Simien, Y. C. Chen, P. Gupta, S. Laha, Y. N. Martinez, P. G. Mickelson, S. B. Nagel, and T. C. Killian. Using absorption imaging to study ion dynamics in an ultracold neutral plasma. *Phys. Rev. Lett.*, 92:14, 2004.

[37] M. Yasuda and H. Katori. Lifetime measurement of the 3p2 metastable state of strontium atoms. *Arxiv: http://arxiv.org/pdf/physics/0310074.pdf.*

[38] G. Zwicknagel. Molecular dynamics simulations of the dynamics of correlations and relaxation in an ocp. *Contrib. Plasma Phys*, 39:155, 1999.